Review article

Cathode materials for rechargeable zinc-ion batteries: From synthesis to mechanism and applications

Changgang Li [a], Xudong Zhang [a,**], Wen He [a,*], Guogang Xu [b], Rong Sun [a]

[a] College of Material Science and Engineering, Qilu University of Technology (Shandong Academy of Sciences), Jinan, 250353, China
[b] College of Material Science and Engineering, Shandong University of Science and Technology, Qingdao, 266590, China

HIGHLIGHTS

- Various cathode materials of zinc-ion batteries are reviewed and summarized.
- Synthesis, composition, electrochemical properties and reaction mechanisms are highlighted.
- Influences of electrolyte and anode on the performances are also analyzed.
- Strategies, recommendations and directions on future research are provided.

GRAPHICAL ABSTRACT
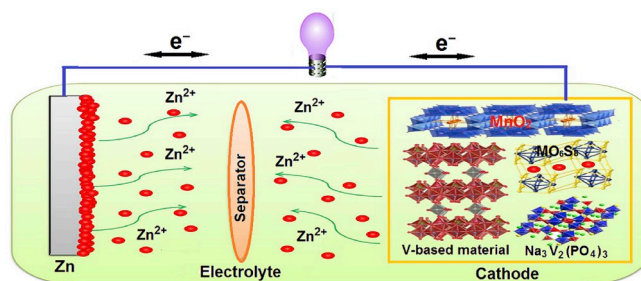
ABSTRACT

Rechargeable zinc-ion batteries (RZIBs) are one of the most promising candidates to replace lithium-ion batteries and fulfill future electrical energy storage demands due to the characters of high environmental abundance, low cost and high capacities (820 mAh g^{-1}/5855 mAh cm^{-3}). Although some progresses have been made in enhancing the electrochemical performance of RZIBs, challenges of the lack of suitable cathodes to tolerate the stable insertion/extraction of Zn^{2+} ions still remain. In this review, we mainly summarize the synthesis technology, composition, structure and electrochemical properties of various cathode materials of RZIBs as well as optimization of the electrolyte, which include manganese-based oxides, vanadium-based materials, Prussian blue analogues, Chevrel phases, polyanionic compounds, metal disulfides, organic compounds, aqueous electrolyte and nonaqueous electrolyte. Furthermore, their energy storage mechanisms are also discussed. Finally, challenges, further research directions and perspectives regarding the development of high performance cathodes are highlighted. This review will be beneficial for researchers to develop high performance RZIBs for meeting the demands of rapidly developing electric vehicles and portable electronic products.

1. Introduction

The development of rechargeable batteries plays a vital role in the energy storage industry. In the past few decades, lithium-ion batteries are widely used for mobile electronics and electric vehicles due to the high energy density and mature markets [1–7]. However, lithium-ion

Table 1

Comparison of the characteristics of zinc metal with those of other metals [13, 14,19,21].

Category	Zn	Li	Na	Mg	K	Al
Cation radius (Å)	0.75	0.76	1.02	0.72	1.38	0.53
Atomic weight (g mol^{-1})	65.41	6.94	22.99	24.31	39.10	26.98
Density (g cm^{-3})	7.13	0.53	0.9	1.74	0.89	2.7
Volumetric capacity (mAh m^{-3})	5857	2042	1050	3868	609	8056
Gravimetric capacity (mAh g^{-1})	820	3861	1166	2205	685	2981
Cost (USD kg^{-1})	2.2	19.2	3.1	2.2	13.1	1.9
Abundance rank	25	33	6	8	7	3
E (*vs.* the SHE) (V)	−0.76	−3.04	−2.71	−2.37	−2.93	−1.76

batteries suffer from complicated issues, such as safety, lack of lithium resources and environmental concerns, which led to the extensive exploration of new battery chemistries. Sodium-ion batteries have been considered as promising alternative to lithium-ion batteries for energy storage applications because of the abundant sodium reserves [8–12]. But it is difficult to find host materials with open structure for reversible Na$^+$ insertion/deintercalate since the larger size and sluggish diffusion kinetics of Na$^+$ as compared to Li$^+$. Developing renewable energy and expanding electric transportation require high energy density, fast charge/discharge time and environmentally friendly battery technology. Therefore, researchers turn their attention to rechargeable multivalent-ion batteries, such as rechargeable zinc-ion batteries (RZIBs) [13–16], magnesium-ion batteries [17,18], calcium-ion batteries [19,20] and aluminum-ion batteries [21,22]. Among them, RZIBs have particularly advantages in the following aspects (Table 1). Firstly, zinc metal is naturally abundant, inexpensive (USD \$2 kg^{-1}), and nontoxic [23]. Secondly, as an anode it offers high gravimetric (820 mAh g^{-1}) and volumetric capacities (5855 mAh cm^{-3}). Moreover, zinc metal can also be used in both organic and aqueous electrolytes. It possesses not only a low redox potential (−0.76 V vs. standard hydrogen electrode) compared to other metal anodes in aqueous electrolytes, but also two-electron transfer mechanism during cycling responsible for the high energy density.

However, the application of RZIBs in practical energy storage devices still face substantial challenges because of the formation of Zn dendritic structures and the passivation layer on Zn electrode during charging, which hinders Zn^{2+} diffusion, resulting in capacity fade, short cycle life, and safety issues [24,25]. In addition, the standard electrode potential of Zn^{2+} ion deposition in aqueous electrolytes is more negative than that for hydrogen evolution, and this could pose a challenge to electrolyte stability in the aqueous phase [26]. In order to restrain the Zn dendrite, coating and morphological optimization for Zn electrode have proven to be very effective strategies. Wang et al. [27] achieved dendrite-free

cycling behavior and flexible negative electrode by electrodepositing Zn on carbon fibers, which offers an efficient solution to inhibit the growth of dendritic zinc. Parker et al. [28] used 3D Zn sponges to elevate the performance of the alkaline Zn//Ni(OH)$_2$ battery, achieving an incredible long cycle life without Zn dendritic formation after ~54000 cycles. Kang et al. [29] prepared a Zn composite anode by mixing zinc particles with activated carbon to improve the cycle performance of RZIBs. Li et al. [30] fabricated a RZIB based on a new intercalated Na$_3$V$_2$(PO$_4$)$_2$F$_3$ cathode coupled with carbon film functionalizing Zn anode and 2 M Zn(CF$_3$SO$_3$)$_2$ electrolyte. The carbon film functionalizing Zn anode was prepared by rolling 80 wt% carbon black (super P) and 20 wt% polytetrafluoroethylene (PTFE) into thin carbon film (thickness, ~0.1 mm) and then placed it on the surface of a Zn foil. These methods mentioned above largely circumvent the plague of dendritic growth. As for the problem of hydrogen evolution in aqueous electrolytes, exploration of organic electrolytes [31] and ionic liquid electrolytes [32] has been reported in RZIBs. However, most of the ionic liquid have imidazolium and pyrrolidinium cations, trifluoromethylsulfonate (TfO$^-$), bis (trifluoromethylsulfonyl)amide (TFSA$^-$) and dicyanamide (DCA$^-$) counter ions, causing their application to be limited by eco-toxicity, biodegradability and biocompatibility [33]. Bio-ionic liquid (choline)--water mixture might be a promising electrolyte for RZIBs because it is nontoxic, cheap and bio-degradable.

The biggest challenge blocking application of RZIBs is the lack of cathode materials with high reversible capacity, excellent cycle stability and adequate operating voltage. Divalent Zn^{2+} ions show strong electrostatic interactions with the host structures and large steric hindrance effects, inducing the poor cyclability and extremely slow intercalation kinetics [34,35]. It is apparent that the design rules for multivalent ions storage/intercalation processes are fundamentally different than that of monovalent ions. Many materials are currently reported as cathode for RZIBs, including manganese-based oxide, vanadium-based materials, Prussian blue analogues, Chevrel phases, polyanionic compounds, metal disulfides and organic compounds.

As seen from Table 2, the number of annual publications on various reviews of RZIBs continues to increase rapidly in the past two years. These reviews mainly focus on the energy storage mechanism, electrochemical activation and challenges of RZIBs as well as recent development of electrode materials. Though few important reviews have summarized the recent advances and prospects of RZIBs from different aspects (Table 2) [13–16,25,31,170], we shall present a different review in order to help readers readily understand the important roles of reasonable design and synthesis technology of cathode materials in improving the electrochemical performances of RZIBs. In this review, we mainly focus on the design and synthesis technology of various cathode materials for RZIBs in aqueous and nonaqueous electrolyte. The synthetic methods, composition, structure, morphologies, electrochemical properties and reaction mechanisms of various cathode materials are

Table 2

Comparison of various reviews of RZIBs.

Published journal	Page number	Title	Highlight point	Ref.
Adv. Funct. Mater.	28 (2018) 1802564	Recent Advances in Zn-Ion Batteries	Crystal structures of cathode materials and Zn ion storage mechanisms	[13]
J. Mater. Chem. A	7 (2019)18209-18236	A review on recent developments and challenges of cathode materials for rechargeable aqueous Zn-ion batteries	Recent developments and challenges of cathode materials	[14]
Mater. Sci. Eng., R	135 (2019)58–84	Zinc-ion batteries: Materials, mechanisms, and applications	Reaction mechanism of cathode materials	[15]
Adv. Sustainable Syst.	3 (2019)1800111	Progress in Rechargeable Aqueous Zinc- and Aluminum-Ion Battery Electrodes: Challenges and Outlook	Mechanisms of electrochemical activation, insertion, and conversion occur	[16]
Adv. Mater. Interfaces	6 (2019)1900387	Recent Advances and Prospects of Cathode Materials for Rechargeable Aqueous Zinc-Ion Batteries	Comprehensive overview and summary of cathode materials	[25]
ACS Energy Lett.	3 (2018)2480-2501	Recent Advances in Aqueous Zinc-ion Batteries	Energy storage mechanisms and types and challenges of cathode materials	[31]
ACS Energy Lett.	3 (2018) 2620−2640	Present and Future Perspective on Electrode Materials for Rechargeable Zinc-Ion Batteries	Challenges and recent developments of Zinc-Ion Batteries	[170]
Our review		Cathode materials for rechargeable zinc-ion batteries: from synthesis to mechanism and applications	Synthesis technology, composition and optimization of cathode materials	

Table 3
Tunnel type and size of different crystallographic forms of MnO₂ [41].

MnO₂ form	Tunnel	Size/Å
α-MnO₂	(1×1), (2×2)	1.89, 4.6
β-MnO₂	(1×1)	1.89
γ-MnO₂	(1×1), (1×2)	1.89, 2.3
δ-MnO₂	interlayer distance	7.0
Todorokite MnO₂	(3×3)	7.0

comprehensively discussed. Reaction mechanisms, including Zn^{2+} insertion/extraction, chemical conversion, H^+/Zn^{2+} co-insertion/extraction, displacement and cation and anion co-intercalation mechanism are systematically analyzed. Moreover, the merits and key issues as well as the optimization strategies related to various cathodes and electrolytes are discussed. Finally, the recently explored cathodes, flexible zinc-ion battery, challenges, recent research trends and directions on cathode materials that can improve the battery performance are also presented. This review hopes to reveal particular strategies which may facilitate future developments of RZIBs.

2. Manganese-based oxide

2.1. MnO₂

Manganese dioxide (MnO₂) has been widely used as cathode materials of various batteries, such as zinc-manganese batteries, lithium-ion batteries and supercapacitors, because it is electrochemically active, environmentally friendly, and relatively cheap [36–40]. In MnO₂ polymorphic crystal structure Mn^{4+} ions occupy octahedral pores formed by

hexagonally close-packed (hcp) oxide ions to form basic MnO_6 octahedral units, and these units are linked by edges and/or corners. The different linkages between the fundamental MnO_6 octahedral units can form various polymorph crystallographic structures [41]. Many polymorphic MnO₂, such as α-MnO₂, β-MnO₂, γ-MnO₂, ε-MnO₂, δ-MnO₂ and todorokite-type MnO₂ have been used in cathode materials of RZIBs up to now. Table 3 is tunnel feature and tunnel size of different MnO₂ forms.

2.1.1. α-MnO₂

Xu et al. [42] prepared α-MnO₂ cathode via a simple self-reacting microemulsion method using KMnO₄ as raw material, iso-octane as solvent and surfactant sodium bis (2-ethylhexyl) sulfosuccinate as reductant. They first proposed a charge storage mechanism established on the migration of Zn^{2+} ions between this cathode and zinc anode in mild ZnSO₄ or Zn(NO₃)₂ aqueous electrolyte (Fig. 1a). This RZIB provides a high capacity of 210 mAh g⁻¹ at 0.5 C, which is higher than the capacity of alkaline Zn/MnO₂ battery (125 mAh g⁻¹) [43]. The discharge capacity is about 100 mAh g⁻¹ at 6C, and the Coulombic efficiency is about 100% after 100 cycles, indicating a high utility of electric capability. The cyclic voltammograms (CV) in Fig. 1b confirmed that the two distinguishable peaks at around 1.3 and 1.7 V are Zn^{2+} ions storage/release into/out of crystalline α-MnO₂ tunnels to form $ZnMn_2O_4$. After that, the group of Xu [44] continued to investigate the storage process of Zn^{2+} insertion into α-MnO₂ by electrochemical impedance spectrum. The results show that the storage process of alkaline (Li⁺, Na⁺, or K⁺) or alkaline-earth (Mg^{2+}, Ca^{2+}, or Ba^{2+}) metal cations in α-MnO₂ can be divided into four steps: (1) transfer of hydrated cations from the electrolyte to the surface of the MnO₂ electrode; (2) hydrated cations migration to the surface MnO₂ particles from the
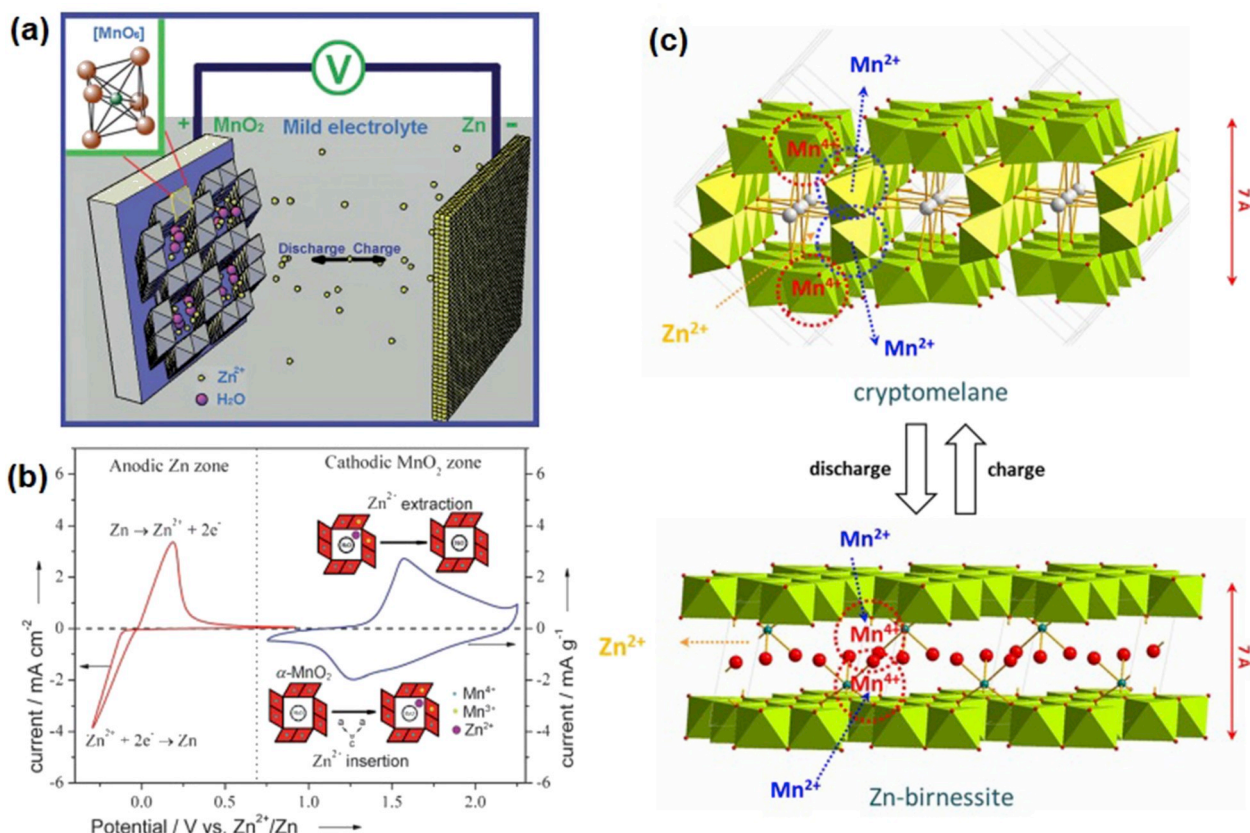

Fig. 1. (a) Schematic diagram of the aqueous RZIB, the inset shows MnO_6 octahedron structure in MnO₂. (b) Cyclic voltammograms of the zinc anode (red line) and the α-MnO₂ cathode (blue line) at 2 mV s⁻¹ in 0.1 mol L⁻¹ Zn(NO₃)₂ electrolyte. Reproduced with permission from Ref. [42], Copyright 2012 Wiley-VCH Verlag GmbH & Co. KGaA, Weinheim. (c) Schematic diagrams illustrating the mechanism of zinc intercalation into α-MnO₂. Green octahedra and white, red, and turquoise spheres represent MnO_6, K⁺, H₂O, and Zn^{2+}, respectively. Reproduced with permission from Ref. [48], Copyright 2014 Springer Nature Limited. (For interpretation of the references to color in this figure legend, the reader is referred to the Web version of this article.)
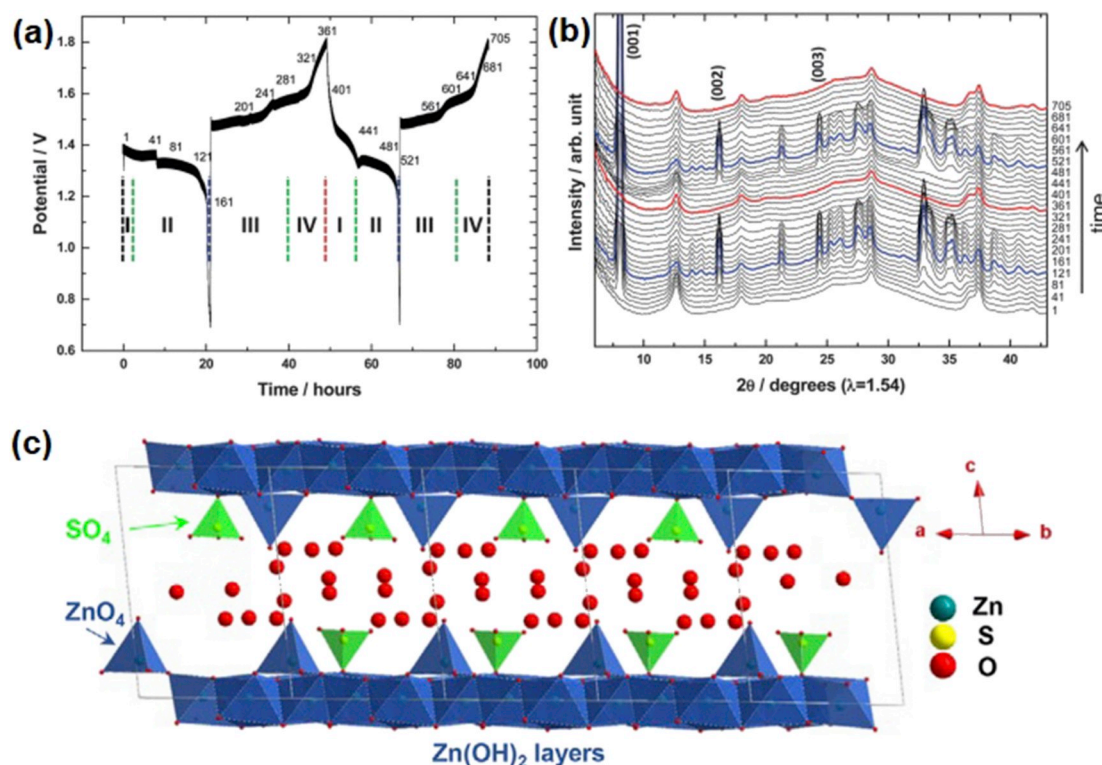
Fig. 2. (a) The charge-discharge profiles of the zinc/α-MnO$_2$ for the first two cycles at a scan rate of C/20 (1C = 210 mA g^{-1} of the active mass). (b) The corresponding *in situ* XRD patterns during the electrochemical cycling. The regions of interest are described as I, II, III, and IV in (a). Reproduced with permission from Ref. [51]. Copyright 2015 The Royal Society of Chemistry. (c) Crystal structure of Zn$_4$(OH)$_6$SO$_4$·5H$_2$O. Reproduced with permission from Ref. [56]. Copyright 2016 Wiley-VCH Verlag GmbH & Co. KGaA, Weinheim.

porous MnO$_2$ electrode; (3) dehydration of hydrated cations at solid/-electrolyte interface; and (4) diffusion of cations in the MnO$_2$ lattice [45–47]. This storage process of Zn^{2+} ions is mainly determined by the phase change while there are no significant phase changes when MnO$_2$ stores alkaline or alkaline-earth metal cations. With the decrease of potential, Zn^{2+} ions insert into MnO$_2$ and form a new ZnMn$_2$O$_4$ phase, which leads to the increase of phase change resistance.

Lee et al. [48] also synthesized a crystalline α-MnO$_2$ nano-rod cathode by hydrothermal method using KMnO$_4$ as raw material at 140 °C for 24 h. They investigated the intercalation mechanism of Zn^{2+} ions into α-MnO$_2$ cathode during discharge/charge reactions, which undergoes a reversible phase transition of MnO$_2$ from tunneled to layered polymorphs. The manganese decomposed from α-MnO$_2$ during discharge process formed layered Zn-birnessite. The structure of Zn-birnessite is most likely an analogue of chalcophanite ((Zn, Mn) Mn$_3$O$_7$·3H$_2$O) with P-1 space group, and the interlayer distance of layered Zn-birnessite is approximately 7 Å [49,50]. The substantial manganese decomposed from the cathode was dissolved into the electrolyte (1.0 M ZnSO$_4$ solution) during discharge process. In discharging process, almost 1/3 manganese in the α-MnO$_2$ electrode is dissolved to form Zn-birnessite. However, the Mn concentration in electrolyte become negligibly small during charging, which means that dissolved Mn^{2+} ions completely recovered to combine with Mn vacancy sites of the layered structure to form the original α-MnO$_2$. The mechanism of zinc intercalation into α-MnO$_2$ is shown in Fig. 1c.

About a year later, Lee et al. [51] also elucidated the intercalation mechanism of zinc ions into α-MnO$_2$ by *in situ* X-ray diffraction (XRD in) more detail. Fig. 2a is charge-discharge profile for the first two successive cycles and Fig. 2b is the corresponding *in situ* X-ray XRD patterns during the cycling. In regions II and III, counter-diffusion between Mn^{2+} and Zn^{2+} ions occurs during the electrochemical process, leading to the emergence of a new phase. In regions I and IV, Zn^{2+} ions diffuse into/out of the 2 × 2 tunnel of α-MnO$_2$, where only one single phase reaction

occur. The result shows that Zn-birnessite is not a direct reaction product of zinc insertion into α-MnO$_2$, but was formed by the loss of the intercalated zinc ions and water molecules from the layers of buserite. Buserite crystallize has the channel width of about 10–11 Å, which is an important precursor of other types of manganese dioxide [52]. In aqueous solution, Zn^{2+} ions are usually octahedrally coordinated with water molecules octahedrons to form [Zn(H$_2$O)$_6$]$^{2+}$ [53]. Owning to the high charge density of central divalent cation, the water molecules in the complex are strongly polarized, which causes hydrolysis to generate [Zn(H$_2$O)$_{6-h}$(OH)$_h$]$^{(2-h)+}$ (h represents the degree of hydrolysis). Since the width of the buserite tunnel is large (about 11 Å), Zn^{2+} ions may move through the channel with [Zn(H$_2$O)$_{6-h}$(OH)$_h$]$^{(2-h)+}$ so that the charge of Zn^{2+} ions is partly shielded. When the amount of Zn^{2+} ions is large, Zn^{2+} ions in layered MnO$_2$ compounds adopt octahedral configurations on the manganese vacancy site coordinated with three oxygen atoms adjacent to vacancy sites and three water molecules inside the channel [54]. When the amount of Zn^{2+} ions is small, the ions are tetrahedral with one water molecule above/below the manganese vacancies [55]. It is known that the structure of buserite has three water layers in the channel, which may help to insert or remove of zinc ions. The large volumetric change between α-MnO$_2$ and Zn-buserite can induce a large amount of residual structural stress during the electrochemical cycle, which leads to collapse of the layered structure during repeated cycles, ultimately resulting in decrease of capacity.

After that, Lee's [56] team also synthesized the α-MnO$_2$ nanorod cathode by using a hydrothermal method through reduction of KMnO$_4$ with NH$_4$Cl and studied the role of pH evolution of aqueous zinc sulfate electrolyte. They found that Zn^{2+} ions precipitated on the surface of α-MnO$_2$ and formed layered zinc hydroxide sulfate (Zn$_4$(OH)$_6$(SO$_4$)·5H$_2$O) (Fig. 2c) instead of intercalate into the tunnels of α-MnO$_2$. The formation of Zn$_4$(OH)$_6$(SO$_4$)·5H$_2$O is dependent on the pH value of the solution. Therefore, they proposed a new reaction mechanism of RZIBs. During the discharge process, the electrochemical reduction of

manganese dioxide on the cathode produces an unstable trivalent manganese, Mn^{3+} ($Mn^{4+} + e^- \rightarrow Mn^{3+}$) due to its high-spin electronic configuration ($d^4 = t_{2g}^3 \,_g^1$) [57,58]. This kind of Jahn-Teller cation is inclined to experience a disproportionation ($2Mn^{3+} \rightarrow Mn^{4+}(s) + Mn^{2+}(aq)$), leading to manganese dissolve into electrolyte [59,60]. And the pH value of the electrolyte will increases, this phenomenon causes crystallization of zinc hydroxide sulfate from the electrolyte on the α-MnO$_2$ surface. Moezzi et al. also reported that zinc hydroxide sulfate precipitated from aqueous ZnSO$_4$ solution when the solution changed from acidic to neutral [61]. Upon charging, due to the recombination of manganese on the cathode, the pH value of the electrolyte starts to decrease and the precipitate dissolve back into the electrolyte. The whole reaction can be written as:

$$3MnO_2 + 3Zn + 5Zn^{2+} + 2SO_4^{2-} + 16H_2O \leftrightarrow 3Mn^{2+} + 2Zn_4(OH)_6(SO_4) \cdot 5H_2O\downarrow \quad [1]$$
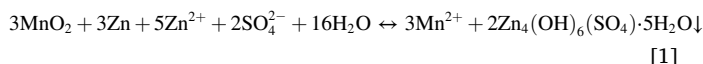
Their work reveals that it is important to construct a highly porous structure in the cathode to accommodate zinc hydroxide sulfate precipitates. Otherwise they may hinder the diffusion of Zn^{2+} and Mn^{2+} ions and further lead to increase of impedance. In the same year, Pan et al. [62] synthesized α-MnO$_2$ nanofibres by a hydrothermal method. The length of α-MnO$_2$ nanofibre extends to a few micrometres, with a diameter of about 50 nm. They presented that α-MnO$_2$ is likely to react with a proton in water to form MnOOH ($MnO_2 + H^+ + e^- \leftrightarrow MnOOH$), which reveals an alternative conversion reaction mechanism between MnOOH and MnO$_2$ other than Zn^{2+} ion intercalation into MnO$_2$. The H^+ ions react with MnO$_2$ in aqueous solution, as a result, the sequent OH^- ions react with ZnSO$_4$ and H$_2$O to form a large flake-like ZnSO$_4$[Zn(OH)$_2$]$_3$·xH$_2$O and reach a neutral charge in the system.

2.1.2. β-MnO$_2$

Earlier, Jiao et al. [63] synthesized mesoporous β-MnO$_2$ with highly intense (110) plane orientation and found that a large amount of Li^+ intercalates and deintercalates easily in its structure to form Li$_{0.92}$MnO$_2$. Su et al. [64] synthesized α-MnO$_2$ and β-MnO$_2$ nano-rods by hydrothermal method using (NH$_4$)$_2$S$_2$O$_8$ and MnSO$_4$·H$_2$O as raw materials, cationic surfactant cetyltrimethylammonium bromide (CTAB) as a soft template at 140 °C for 12 h. When applied β-MnO$_2$ nano-rods as a cathode of sodium-ion batteries, it exhibits better electrochemical performances such as good rate capability and cyclability than that of α-MnO$_2$ nanorods, which ascribe to more compact tunnel structure of β-MnO$_2$ nanorods. Therefore, β-MnO$_2$ with large open tunnels also is one of the most promising cathode materials for RZIBs due to the similar ionic radius of Zn^{2+} (74 p.m.) with Li^+ (76 p.m.). Islam et al. [65] prepared β-MnO$_2$ nanorod with exposed (101) planes through rapid microwave-assisted hydrothermal method using KMnO$_4$ and MnSO$_4$ as raw materials at 200 °C for 10 min, and applied as the cathode material for RZIB for the first time. This β-MnO$_2$ nanorod electrode exhibited a high discharge capacity of 270 mAh g^{-1} at 100 mA g^{-1}, high rate capability (123 and 86 mAh g^{-1} at 528 and 1056 mA g^{-1}, respectively), and long cycling stability (75% capacity retention with 100% Coulombic efficiency at 200 mA g^{-1}) over 200 cycles. The results also showed that the cycle stability of β-MnO$_2$ nanorods was significantly improved by adding MnSO$_4$ in aqueous ZnSO$_4$ electrolyte. Concerning the reaction mechanism of β-MnO$_2$, they supposed that Zn^{2+} ions intercalated into β-MnO$_2$ framework and formed spinel ZnMn$_2$O$_4$ Zn-inserted phase, meanwhile ZnSO$_4$·3Zn(OH)$_2$·5H$_2$O deposited on the electrode surface. And during Zn^{2+} ions insertion, the lattice spacing of (101) plane of β-MnO$_2$ undergoes a slight expansion. Therefore, tailoring crystal orientation for electrode material can promote facile ionic transports during electrochemical reaction, which is a promising strategy for the application of energy storage. Zhang et al. [66] designed a high-performing RZIB system based on zinc anode, β-MnO$_2$ cathode, and 3 M Zn(CF$_3$SO$_3$)$_2$+0.1 M Mn(CF$_3$SO$_3$)$_2$ aqueous electrolyte. The β-MnO$_2$ nanorod cathode was synthesized by a hydrothermal method using

KMnO$_4$ and MnSO$_4$·H$_2$O as raw materials at 140 °C for 12 h. This battery exhibits high capacity of 225 mAh g^{-1} at 0.65 C, high rate capability of 100 mAh g^{-1} at 32.50 C and long term cycling stability (94% capacity retention after 2000 cycles at 6.50 C).

2.1.3. γ-MnO$_2$

Zeng et al. [67] synthesized a sea-urchin shaped γ-MnO$_2$ electrode using a facile hydrothermal method without employing any template or surfactant with mild conditions. This electrode delivered more than 100 mAh g^{-1} at a high current density of C/3 with high reversibility and good capacity retention after 20 cycles for lithium-ion battery. Mathew et al. [68] synthesized a self-assembled mesoporous γ-MnO$_2$ electrode via ambient temperature redox synthesis at 200 °C, which registered an initial discharge capacity of 268 mAh g^{-1} with a well-defined plateau around 3 V in Li/MnO$_2$ battery. In the field of sodium-ion batteries, Chae et al. [69] synthesized γ-MnO$_2$ nanowire crystallites with diameters and lengths in the range of 2–3 and 25–40 nm by using the previous synthesis method. When employed in sodium-ion battery, this cathode presents initial discharge and charge capacities of 234 and 233 mAh g^{-1} with almost 100% Coulombic efficiency.

Alfaruqi et al. [70] prepared mesoporous γ-MnO$_2$ cathode with high surface area by a simple ambient temperature strategy followed by low-temperature annealing at 200 °C. When used in a RZIB, it delivers an initial discharge capacity of 285 mAh g^{-1}at 0.05 mA cm^{-2} with a defined plateau at around 1.25 V vs Zn/Zn^{2+}. Moreover, the structural transformation of mesoporous γ-MnO$_2$ cathode during electrochemical reaction was intensively investigated by *in situ* XRD and *in situ* Synchrotron X-ray absorption near edge spectroscopy (XANES). The results indicate that the structural transformation of mesoporous γ-MnO$_2$ cathode forms tunnel-type γ-Zn$_x$MnO$_2$ and layered-type L-Zn$_y$MnO$_2$ during the electrochemical reaction, and these phases with multi-oxidation states coexist after complete electrochemical Zn-insertion. More specifically, a part of the orthorhombic γ-MnO$_2$ is converted into spinel-type ZnMn$_2$O$_4$ in the initial stage. The 1 × 1 tunnel in the pyrolusite block of the γ-MnO$_2$ structure is mainly converted into a spinel-type phase, which consistent with the result of Li-insertion in β-MnO$_2$ [71]. With the further progress of discharge reaction, the 1 × 2 tunnels in the domains that retain the parent orthorhombic structure become infiltrated and occupied by zinc, thus tending to expand the geometric dimension of the tunnels and form a new γ-Zn$_x$MnO$_2$ phase. During the later stages of discharge reaction, some of the fully inserted tunnels expand further and open up the structure as more Zn-insertion occurs, eventually forming a layered-type MnO$_2$ with a larger d-spacing (7.26 Å). When the Zn-insertion is completed, the spinel-type ZnMn$_2$O$_4$, tunnel-type γ-Zn$_x$MnO$_2$, and layered-type Zn$_y$MnO$_2$ phases coexist and this process accompany by the reduction of manganese from Mn(IV) to the Mn(III) and Mn(II) states. During the subsequent charging or Zn-deintercalation process, the layered-type polymorph tends to become compressed and revert back to the parent orthorhombic lattice of γ-MnO$_2$. The result of *ex situ* high resolution-transmission electron microscopy (HR-TEM) also confirms the structure transformation of γ-MnO$_2$ during electrochemical reaction.

2.1.4. Akhtenskite MnO$_2$ (ε-MnO$_2$)

Regarding the reaction mechanism of MnO$_2$ in neutral or mild acidic aqueous electrolytes, there is still uncertain and remains controversial. Several works demonstrated that the capacity of MnO$_2$ in aqueous electrolytes is induced by the reversible Zn^{2+} insertion/extraction [42, 48,51]. Lee et al. investigated the reaction mechanism of α-MnO$_2$ cathode in an aqueous zinc sulfate electrolyte by monitoring structural changes. The result shows that Zn^{2+} ions mostly precipitate on the surface of the electrode or in the porosity between the particles to form zinc hydroxide sulfate, rather than intercalating into the tunnels of MnO$_2$ [56]. Pan et al. showed a different reaction mechanism of α-MnO$_2$ cathode which supported the reversible H^+ insertion/extraction to form MnOOH [62]. Sun et al. [72] prepared the binder free Akhtenskite MnO$_2$
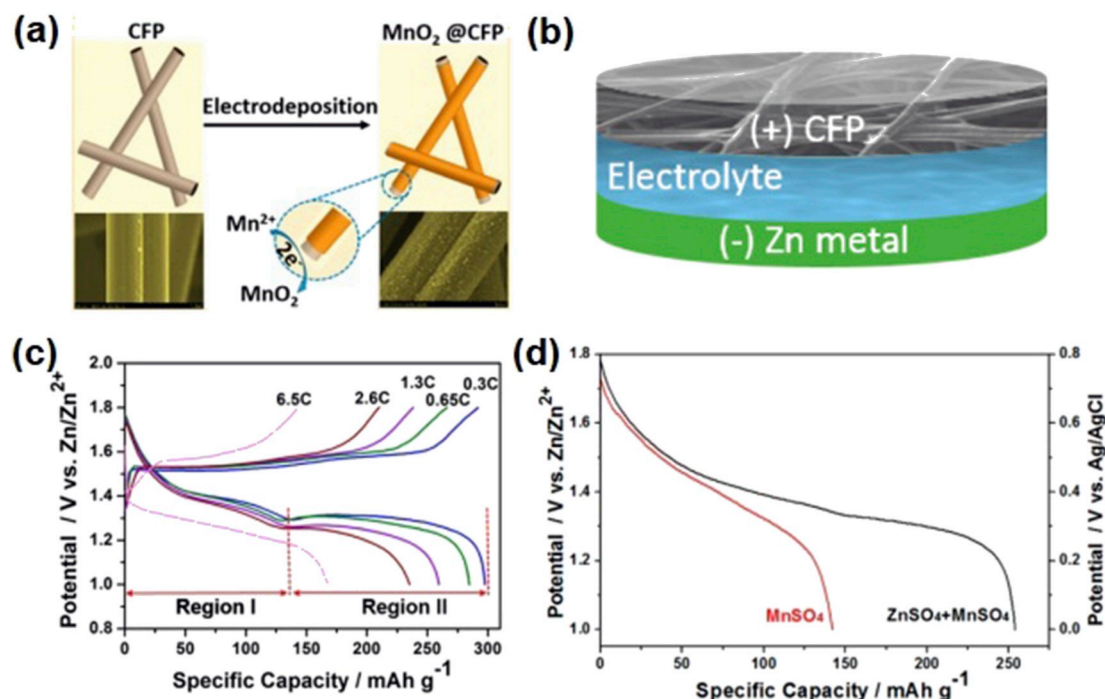
Fig. 3. (a) Schematic illustration of the nanocrystalline MnO_2 electrodeposited on carbon fiber paper (CFP) process, and the corresponding SEM images of CFP before and after electrodeposition. (b) Schematic illustration of the Zn/CFP battery in $ZnSO_4+MnSO_4$ aqueous electrolyte before MnO_2 deposited on CFP. (c) Charge and discharge curves at different rates in first cycle. (d) Discharge curves of MnO_2@CFP cathode in 0.2 M $MnSO_4$ solution with or without $ZnSO_4$ as electrolytes at 0.3 C between 0 and 0.8 V (vs Ag/AgCl) in a three electrode cell. Reproduced with permission from Ref. [72]. Copyright 2017 American Chemical Society.

cathode by *in situ* electrodeposition of MnO_2 on carbon fiber paper (MnO_2@CFP) and designed a highly reversible RZIB in mild acidic $ZnSO_4+MnSO_4$ electrolyte. And they first proposed the mechanism of the consequent H^+ and Zn^{2+} insertion mechanism. The electrodeposited MnO_2 has a nanocrystalline structure and the particle size is typically less than 10 nm. The small particles offer a relatively large electrode/electrolyte contact area and therefore tend to enhance the diffusion kinetics by reducing the diffusion pathway for electronic and ionic transport. Fig. 3a is the illustration of the nanocrystalline MnO_2 electrodeposited on carbon fiber paper (CFP) and Fig. 3b is a schematic diagram of the composition of this battery in $ZnSO_4+MnSO_4$ aqueous electrolyte. This MnO_2@CFP cathode shows a considerably high capacity of 290 mAh g^{-1} at 0.3 C, close to the theoretical capacity of MnO_2 (308 mAh g^{-1}, based on molecular weight of MnO_2 and 1 e^- transfer reaction). At the rate of 1.3C, it exhibits an initial discharge capacity of 260 mAh g^{-1} and maintains 150 mAh g^{-1} after 20 cycles. Even at a high rate of 6.5 C, MnO_2@CFP cathode can provide a stable capacity of 50–70 mA h g^{-1} for 10000 cycles, the corresponding Coulombic efficiency is nearly 100%. Fig. 3c is the charge and discharge curves of this battery at different rates in the first cycle. With the increase in charge and discharge rate, the voltage and capacity drop in the first voltage plateau (region I, ~1.4 V) are very small, whereas both the voltage and capacity in the second voltage plateau (region II, ~1.3 V) significantly declined, indicating that the reaction kinetics in region I is much faster than the reaction in region II. Results of galvanostatic intermittent titration technique (GITT) and electrochemical impedance spectroscopy (EIS) reveal that the total overvoltage in region II is 0.6 V, which is almost 10 times than that of in region I (0.08 V) and the charge transfer and diffusion resistance in the region II is much larger than the charge transfer and diffusion resistance in region I. Since the size of H^+ is much smaller than Zn^{2+}, they conclude that region I takes place H^+ insertion process, whereas the voltage plateau in region II is mainly attributed to the Zn^{2+} insertion. Electrochemical behavior of MnO_2@CFP cathode in 0.2 M $MnSO_4$ electrolyte without $ZnSO_4$ further confirms this hypothesis (Fig. 3d). Since the absence of Zn^{2+}, the flat plateau of 1.3 V in region II

vanishes, only one sloped plateau from 1.8 to 1.35 V appear (H^+ insertion), which demonstrates that the main reaction in region II is caused by Zn^{2+} insertion. *Ex situ* XRD measurements are conducted on MnO_2@CFP electrode after discharge to 1.3 and 1.0 V and maintain at 1.3 and 1.0 V for 24 h to identify the equilibrium phase in regions I and II. Typical MnOOH and $ZnMn_2O_4$ equilibrium phase are observed by *ex situ* XRD measurements further strongly support the mechanism that the MnO_2@CFP cathode experiences H^+ insertion followed by Zn^{2+} insertion.

2.1.5. δ-MnO_2

Based on previous researches of tunnel-type α- and γ-MnO_2 polymorphs in RZIB, Alfaruqi et al. [73] turned their attention to the layered type δ-MnO_2 polymorph with a large interlayer (~7.0 Å). They fabricated a δ-MnO_2 cathode with flake-like morphologies via the simple low temperature thermal decomposition of $KMnO_4$. The Zn/δ-MnO_2 battery assembled with the nano-flake δ-MnO_2 cathode under atmospheric condition exhibits an open-circuit voltage (OCV) of about 1.49 V, discharge capacities as high as 250 mAh g^{-1} under a current density of 83 mA g^{-1} and a Coulombic efficiency of nearly 100% during 100 cycles. Furthermore, the reaction mechanism of the δ-MnO_2 cathode was studied by using the *ex situ* XRD and inductively coupled plasma (ICP). The results reveal that the δ-MnO_2 undergoes a structural transformation to form spinel-type $ZnMn_2O_4$ with Mn (III) state and layered-type δ-Zn_xMnO_2 with Mn (II) phase. Nevertheless, no irreversible phases, such as MnOOH, $Mn(OH)_2$, Mn_3O_4, Mn_2O_3 and ZnO are observed after the discharge reaction, which means there's no side reactions occurring in the cathode.

Han et al. [74] reported a new RZIB system based on δ-MnO_2 ($K_{0.11}MnO_2·0.7H_2O$) cathode, Zn metal anode and nonaqueous acetonitrile-Zn(TFSI)$_2$ electrolyte. The nanostructured $K_{0.11}MnO_2·0.7H_2O$ cathode material was synthesized using a low temperature water-based synthetic route. A great deal of research has been demonstrated that the nonaqueous acetonitrile-Zn(TFSI)$_2$ electrolytes can support highly reversible Zn deposition behavior on a Zn metal anode (≥99% of
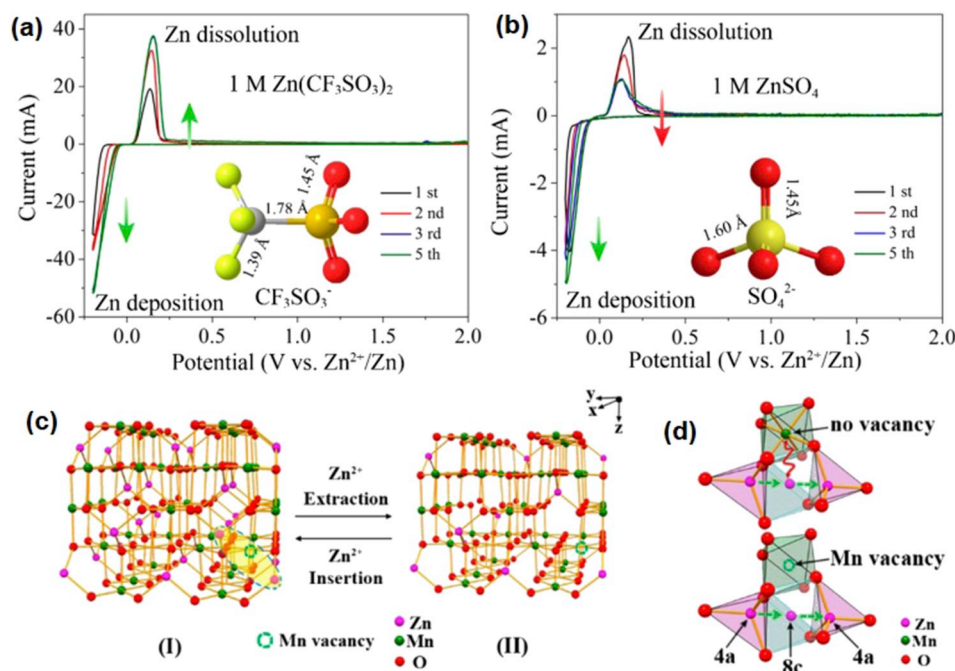
Fig. 4. (a) Cyclic voltammogram (CV) curves of Zn electrode in 1 M $Zn(CF_3SO_3)_2$ at the scan rate of 0.5 mV s^{-1} between −0.2 and 2.0 V. (b) CV curves of Zn electrode in 1 M $ZnSO_4$ at the scan rate of 0.5 mV s^{-1} between −0.2 and 2.0 V. (c) Schematic illustration of Zn^{2+} insertion/extraction in an extended three-dimensional $ZnMn_2O_4$ spinel framework. (d) Proposed Zn^{2+} diffusion pathway in $ZnMn_2O_4$ spinel without and with Mn vacancies. Reproduced with permission from Ref. [86]. Copyright 2016 American Chemical Society.

Coulombic efficiency) with wide electrochemical window (up to 3.8 V vs. Zn/Zn^{2+}) [75–77]. This new RZIB system exhibits a high capacity of 123 mAh g^{-1} after 125 cycles at a current density of 12.3 mA g^{-1} with good reversibility (>99% Coulombic efficiency) and an operating voltage of 1.25 V (vs Zn/Zn^{2+}). The study results of transmission electron microscopy (TEM), element mapping and *ex situ* XRD analysis show that the layer-type δ-MnO$_2$ cycles reversibly between the pristine material and Zn$_x$MnO$_2$ (x$_{max}$ = ~0.2) when Zn^{2+} ions insert into the host material during discharging. At the same time, the Zn^{2+} ions insertion process accompanied by a competing side reaction to irreversible formation of ZnO. However, the amount of ZnO does not apparently increase during cycling, which indicate that it is not only from lattice breakdown, but may be partially derived from the reaction with water or a disproportionation reaction of Zn$_x$MnO$_2$ in the bulk. Thus, the whole reaction can be written as:

$$xZn + K_{0.01}MnO_2 \cdot 0.7H_2O \leftrightarrow Zn_xK_{0.01-y}MnO_2 + yK^+ + 0.7H_2O \quad [2]$$
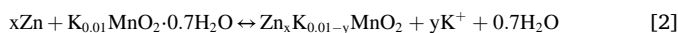
2.1.6. Todorokite-type MnO$_2$

Todorokite-type MnO$_2$ is a new cathode material for RZIB and has the crystallographic structure with1-dimensional 3 × 3 tunnels through the b-axis, which is the largest tunnel among other tunnel-type MnO$_2$ polymorphs (α-MnO$_2$ with a [2 × 2] tunnel, β-MnO$_2$ with a [1 × 1], γ-MnO$_2$ with a mix of [2 × 1] and [1 × 1] tunnel and δ-MnO$_2$ with [1 × ∞] tunnel). Many cations, including alkali, alkaline-earth, transition-metal ions, and even post-transition metal ions and water molecules, can intercalate into this large tunnel, giving an approximate composition of M$_{1+x}$Mn$_6$O$_{12}$·3–4H$_2$O (M = Na, Ca, Mg, Ba, K etc.) [78]. Wei et al. [79] synthesized α-, β-, γ-, and δ-types MnO$_2$ with different tunnel structures and morphologies by a common liquid co-precipitation method based on the redox reactions of Mn^{4+} and Mn^{2+}. They studied the effect of the tunnel structures and morphologies on the storage properties of Zn^{2+} ions, and found that large tunnel structure is favorable to store Zn^{2+} ion. Lee et al. [80] synthesized todorokite-type MnO$_2$ cathode by the hydrothermal treatment of layered Na-birnessite in a concentrated Mg-containing solution and investigated its structural and electrochemical properties. The todorokite-type MnO$_2$ cathode for RZIB delivered a discharge capacity of 108 mAh g^{-1} at C/2 and good rate performance in the potential range of 0.7–2.0 V. Electrode reaction on the cathode can be written as:

$$Mg_{1.8}Mn_6O_{12} \cdot 4.8H_2O + 1.2Zn^{2+} + 2.4e^- = Zn_{1.2}Mg_{1.8}Mn_6O_{12} \cdot 4.8H_2O$$

$$[3]$$
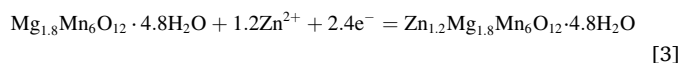
2.2. Spinel ZnMn$_2$O$_4$

Spinel-type ZnMn$_2$O$_4$ has been investigated extensively as the anode materials for lithium-ion batteries [81,82]. ZnMn$_2$O$_4$ is also a promising candidate cathode material for aqueous RZIB because Li$^+$ and Zn^{2+} have almost the same ionic radius. Knight et al. [83] investigated the chemical extraction of Zn from the spinel ZnMn$_2$O$_4$ and found that the ideal spinel structure is not suitable as a RZIB cathode due to the large electrostatic repulsion while the Zn^{2+} ions diffuse through the lattice. In order to reduce the electrostatic repulsion, they suggest creating vacancies to allow for easier Zn^{2+} ions diffusion in the structure through controlling synthesis conditions or additional treatments. Koketsu et al. [84] introduced plenty of charge-compensating titanium vacancies (22%) in anatase TiO$_2$ through aliovalent ion doping to realize the reversible insertion of multivalent ions (Mg^{2+} and Al^{3+}). Sánchez et al. [85] studied the electrochemical insertion of Mg^{2+} into the cation-deficient mixed spinel oxide Mn$_{2.15}$Co$_{0.37}$O$_4$. The cation vacancies in the mixed oxide offer a route for Mg^{2+} insertion with a maximum absorption of 0.23 Mg per mole of oxide.

Inspired by the above works, Zhang et al. [86] reported cation-defective ZnMn$_2$O$_4$/carbon (60 wt% spinel and 40 wt% carbon) composite as cathode material of aqueous RZIBs. The composition of spinel in cation-defective ZnMn$_2$O$_4$/carbon can be written as ZnMn$_{1.86}$Y$_{0.14}$O$_4$ (where the Y represents vacancy). The abundant cation vacancy character is caused by the mild solution-based synthesis (a low temperature of 180 °C and a short time of 3 h), which helps to form the ultrafine and nonstoichiometric spinels [87]. They also investigated the electrochemical properties of ZnMn$_2$O$_4$/carbon in four mild acidic ZnCl$_2$, ZnNO$_3$, ZnSO$_4$ and Zn(CF$_3$SO$_3$)$_2$ aqueous electrolytes. Fig. 4a and b are CV curves of Zn electrode in aqueous electrolyte of 1 M Zn (CF$_3$SO$_3$)$_2$ and 1 M ZnSO$_4$. The results showed that Zn(CF$_3$SO$_3$)$_2$ has better reversibility and faster kinetics of Zn^{2+} deposition/dissolution, which attributes to the bulky CF$_3$SO$_3^-$ anion lessening the number of water molecules around Zn^{2+} and the solvation effect, promoting Zn^{2+} migration and charge transfer.

Previous studies on Li batteries have proved that higher salt concentration can reduce the water activity and water-induced side reactions, thereby enhancing cycle stability and kinetics in aqueous solutions [88,89]. For the $Zn(CF_3SO_3)_2$ electrolyte (pH ≈ 3.6) with concentration of 3 M, the O_2 evolution potential was suppressed to 2.5 V. More importantly, there are no detectable side reactions in the working voltage window of aqueous RZIB (0.8–1.9 V). This cation-defective $ZnMn_2O_4$/carbon composite delivers initial specific charge and discharge capacities of 128 and 120 mAh g^{-1} at the current rate of 50 mA g^{-1} between 0.8–1.9 V.

Even at a high current rate of 2000 mA g^{-1}, the discharge capacity can reach to 72 mAh g^{-1}. In addition, considerable capacity retention of 94% after 500 cycles at high rate of 500 mA g^{-1} is attained. They do some morphological studies on the cathode and anode after 50 cycles. The results reveal that the spinel nanoparticles of $ZnMn_2O_4$/carbon cathode are still firmly anchored on and uniformly composited with carbon, and Zn anode shows a dendrite-free and dense surface morphology. They suggest that the excellent electrochemical performance of $ZnMn_{1.86}Y_{0.14}O_4$ cathode is derived from the rich Mn vacancies, which benefit for Zn^{2+} diffusion in the spinel framework. Upon charging or discharging, Zn^{2+} ions extract or insert from the Zn–O tetrahedral sites of $ZnMn_2O_4$ spinel (Fig. 4c and d). And the electrochemical reaction can be written as $ZnMn_{1.86}Y_{0.14}O_4 \leftrightarrow Zn_{1-x}Mn_{1.86}Y_{0.14}O_4 + 2xe^- + xZn^{2+}$ (0 < x < 1), where x represents the number of reversible extraction of Zn^{2+} and maximum is 0.7 in their study.

Wu et al. [90] reported a hollow porous $ZnMn_2O_4$ cathode for the green-low-cost aqueous RZIB. This cathode is synthesized through a solvothermal carbon template method firstly, followed by an annealing process at 600 °C for 4 h in air. The carbon microsphere template is prepared by using glucose as raw material at 180 °C. And the hybrid electrolyte was synthesized by dissolving zinc sulfate and manganese sulfate in deionized water. This system exhibits reversible discharge capacity of 106.5 mAh g^{-1} at 100 mA g^{-1} after 300 cycles without capacity decay. At the same time, it displayed a high capacity of 70.2 mAh g^{-1} at high current density of 3200 mA g^{-1}, which can be attributed to the mesoporous structure and residual carbon distribution facilitating the charge transfer and shortening the ion diffusion path lengths.

Overall, great advances have been made in synthesis technology and energy storage mechanism researches of manganese-based cathode materials. The various manganese-based cathode materials, such as α-MnO$_2$, β-MnO$_2$, γ-MnO$_2$, ε-MnO$_2$, δ-MnO$_2$, todorokite-type MnO$_2$ and Spinel $ZnMn_2O_4$ have been synthesized by using different synthesis technologies, including microemulsion, hydrothermal, low-temperature thermal decomposition, *in situ* electrodeposition, liquid co-precipitation method and solvothermal carbon template method. However, there are many drawbacks for these synthesis technologies that have not yet been resolved. So new synthesis technologies reducing the manufacturing costs need to be developed for ZIBs to become commercial products. For the reaction mechanism of Mn-based cathodes, there are still many missing details that are yet to be revealed, for example, the variation in the Mn oxidation state is still not clear. Especially the manganese-based cathode materials still suffer the problem of fast capacity decay during the cycling due to dissolution of Mn^{2+} from Mn^{3+} disproportionation into mild acidic aqueous electrolytes.

2.3. Dissolution of manganese-based oxide

Metal oxide cathodes generally suffer from the dissolution of metals during the battery operation because of the commonly used (slightly) acidic electrolytes. The technique used to monitor the dissolution of manganese-based oxide and the structural evolution has been researched widely. Some effective solutions to this problem including surface coating, electrolyte optimization, as well as composition tuning are proposed also. Pan et al. [62] monitored the dissolution of

manganese-based oxide and the structural evolution by analyzing the Mn concentration in electrolyte solution and electrochemical performances through inductively coupled plasma (ICP) and CV techniques. They found that adding 0.1 M MnSO$_4$ additive into the mild ZnSO$_4$ aqueous electrolyte can change the dissolution equilibrium of Mn^{2+} from the MnO$_2$ electrodes, suppress continuous Mn^{2+} dissolution and greatly improves the capacity decay. Moreover, the MnSO$_4$ additive in electrolyte the do not affect the redox reactions in the MnO$_2$ electrode. This battery achieves a higher capacity of 260 mAh g^{-1} at current rates of 1C, excellent rate capability (207, 161 and 113 mAh g^{-1} at 2C, 5C and 10C) and excellent long cycle stability with high capacity retention of 92% after 5000 cycles at 5C.

Adding conductive additives, surface coating and metal ion doping are also effective measures to solve these problems. Wang et al. [91] synthesized carbon-coated α-MnO$_2$ nanoparticles (α-MnO$_2$@C) using maleic acid (C$_4$H$_4$O$_4$) as a carbon source and applied as a cathode material for aqueous ZIB. The test results show that the carbon coating on the electrode material not only increases the electrical conductivity and discharge capacity but also improves the electrode stability and capacity retention by preventing dissolution of manganese from the MnO$_2$ during the electrochemical discharge reaction. Wu et al. [92] proposed highly reversible aqueous RZIB using graphene scroll-coated α-MnO$_2$ nanowires as the cathode to increase the electrical conductivity and relieve the dissolution of the cathode material during cycling. This battery exhibited considerable specific capacity of 145.3 mAh g^{-1} at 3 A g^{-1} with high retention of 94% after 3000 cycles. Yadav et al. [93] reported the development of Cu^{2+}-intercalated layered MnO$_2$ cathodes. Cu is used as an intercalant to improve the electrochemical properties of layered structure MnO$_2$. This cathode exhibited a capacity of 617 mAh g^{-1} for over 900 cycles. In addition, Xu et al. [94] synthesized MnO$_2$/carbon nanotube (CNT) nanocomposites by a simple co-precipitation method for improving electrical conductivity and stabilize electrode. This MnO$_2$/CNT anode delivered excellent Zn^{2+} storage properties (~400 mAh g^{-1} at 1 A g^{-1}) and reversibility (~100% Coulombic efficiency after 500 charge/discharge cycles). In short summary, these solutions can not only efficiently suppress Mn dissolution from the MnO$_2$ electrode but also improves the electrode stability and capacity retention.

3. Vanadium-based materials

Vanadium (V)-based cathodes with different frameworks for RZIBs have advantages of stability and diversity by contrast with Mn-based cathodes. V–O coordination polyhedral can adopt different units and can be constructed by corner and/or edge sharing of these polyhedral. The frameworks of Vanadium-based cathodes allow for reversible Zn^{2+} intercalation/deintercalation [15]. The V-based cathodes include vanadium pentoxide (V$_2$O$_5$), M$_x$V$_2$O$_5$ (M = Na, Ca, Zn, Mg, Ag, Li …) and other layered and tunnel-type vanadium-based compounds.

3.1. V$_2$O$_5$

V$_2$O$_5$ is found to be a successful candidate for storage of larger multivalent metal-ions, such as Mg^{2+} [95], Al^{3+} [96] and Zn^{2+} because its layered structure has the large spacing. Zhou et al. [97] synthesized low-cost V$_2$O$_5$ nanoparticle cathode by a wet chemistry method reported at 400 °C in air for 2 h. They investigated the influence of different type of the aqueous electrolytes (ZnSO$_4$, Zn(CH$_3$COO)$_2$, Zn(NO$_3$)$_2$ and ZnCl$_2$) on the electrochemical performances of this Zn/V$_2$O$_5$ system. The results show that the V$_2$O$_5$ nanoparticle cathode in 3 M ZnSO$_4$ electrolyte delivered a high specific of 224 mAh g^{-1} at 100 mA g^{-1}, and an excellent long-term cycling performance up to 400 cycles at 2 A g^{-1}. The ZnSO$_4$ electrolyte can achieve the better reversibility and faster kinetics of Zn deposition/dissolution [86]. Hu et al. [98] develop a novel hybrid-ion battery system by using porous V$_2$O$_5$ as the cathode and metallic zinc as the anode as well as a new "water-in-salt" electrolyte (21 M lithium
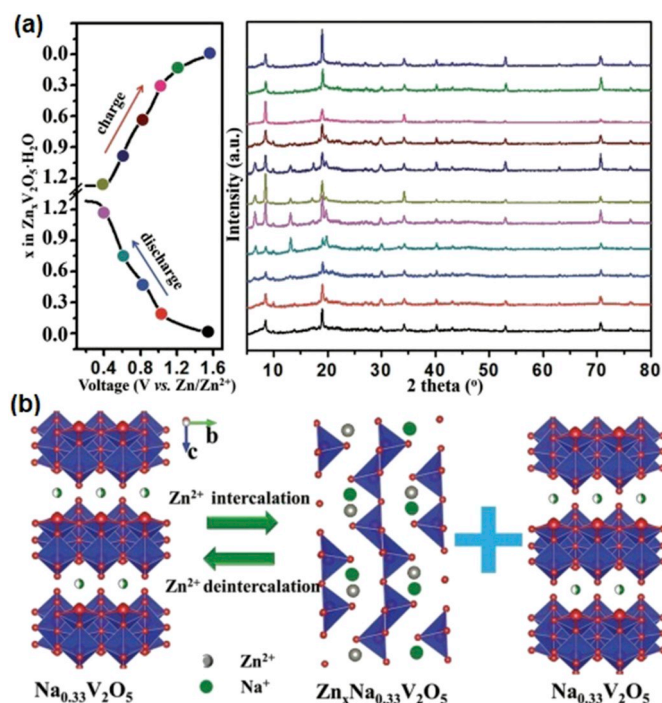
Fig. 5. (a) XRD patterns of $V_2O_5 \cdot nH_2O$ at different charge and discharge states. Reproduced with permission from Ref. [105]. Copyright 2017 WILEY-VCH Verlag GmbH & Co. KGaA, Weinheim. (b) Schematic illustration of the zinc-storage mechanism in the $Na_{0.33}V_2O_5$ electrode. Reproduced with permission from Ref. [109]. Copyright 2018 WILEY-VCH Verlag GmbH & Co. KGaA, Weinheim.

bis(trifluoromethane sulfonyl)imide (LiTFSI) and 1 M $Zn(CF_3SO_3)_2$). The "water-in-salt" electrolyte is able to retard the hydrogen and oxygen evolution at a high electrochemical window (~3.0 V) in this Zn/V2O5 battery [99,100]. The porous V_2O_5 cathode delivers a high discharge capacity of 238 mAh g^{-1} at 50 mA g^{-1} and 80% of the initial discharge capacity can be retained after 2000 cycles at a high current density of 2000 mA g^{-1}. More importantly, the discharge platform increase from 0.6 to 1.0 V. Moreover, they confirmed the intercalation reaction mechanism of Zn^{2+} ions in V_2O_5 by using *ex-situ* X-ray photoelectron spectroscopy (XPS) and HR-TEM test. The results show that Zn^{2+} ions can be successfully intercalated into V_2O_5 after discharged to 0.2 V, which leads to the increase of (200) lattice spacing (2.43%), but not all the Zn^{2+} ions can be de-intercalated after recharging to 1.6 V. They assume that the captured Zn^{2+} ions may act as the interlayer pillars and stabilize the layered structure of V_2O_5 during the charge/discharge processes, which is similar to the effects of pre-intercalated metal ions (Li^+, Na^+, K^+, Zn^{2+} …) in V_2O_5 [101]. This work provides an effective method to enhance the energy density and long-term cycling stability of zinc-ion based aqueous batteries.

Senguttuvan et al. [102] synthesized a hydrated bilayered V_2O_5 (BL-V_2O_5) cathode with a large gallery spacing of 11–13 Å by electrochemical deposition on carbon substrate with good porosity. The OCV of this Zn/V_2O_5 battery in nonaqueous acetonitrile (AN)-$Zn(TFSI)_2$ electrolyte is 1.42 V vs Zn^{2+}/Zn, and approximately 0.59 mol of Zn^{2+} can be inserted per mole of V_2O_5, which leads to reduced gallery spacing. This phenomenon of gallery spacing was demonstrated by the fact that Mg^{2+} ions can be effectively intercalated into interlayer spacing of BL-V_2O_5 [103]. The BL-V_2O_5 cathode delivers stable capacities of ≈170 mAh g^{-1} for 120 cycles with a Coulombic efficiency of 83.7% at C/10. Even at a high rate of 20 C, it also exhibits a capacity of 130 mAh g^{-1}. The Capacity decay at high rate can be attributed to morphological changes, electrochemical polishing phenomena, and loss of electronic contact of the active material with the carbon substrate [104]. They also speculate

that water molecules in oxide lattice layers act as coordinating and stabilizing molecules, which contribute to fast Zn^{2+} ion diffusion.

Later, Yan et al. [105] investigated the critical role of structural H_2O on Zn^{2+} intercalation into bilayer $V_2O_5 \cdot nH_2O$ (n ≥ 1) in 3 mol L^{-1} Zn $(CF_3SO_3)_2$ electrolyte in detail. The results show that the H_2O-solvated Zn^{2+} possesses largely reduced effective charge, thereby reducing electrostatic interactions with the host material framework and effectively promoting its diffusion. The XRD patterns (Fig. 5a) of $V_2O_5 \cdot nH_2O$ at different charge and discharge states show that Zn^{2+} ions are extracted from the interlayer during the charging process, and the interlayer spacing of bilayer V_2O_5 changes from 12.6 to 10.4 Å after charging to 1.3 V. There are two stages for the discharge process. The first discharge redox appears at about 1.1–0.8 V accompany with 0.3 mol Zn^{2+} ions intercalation. The second discharge redox happens in the voltage range of 0.6–0.4 V. It is found that a new phase with the interlayer distance of 13.5 Å is formed due to the intercalation of Zn^{2+} ions. Since the water-based shielding layer reduces the "effective charge" of Zn^{2+} and increases the distance between Zn^{2+} and the neighboring oxygen ions (r_0), the interlayer distance of bilayer V_2O_5 increases from 10.4 to 13.5 Å due to Zn^{2+} intercalation. The results of the solid-state magic-angle-spinning (MAS) nuclear magnetic resonance (NMR) also indicate that water is highly involved in the battery charge/discharge processes and plays an important role. Nam et al. [106] adopted the same strategy to introduce crystal water (~10 wt%) into the layered MnO_2 cathode of aqueous RZIB. The interlayer crystal water can effectively screen the electrostatic interactions between Zn^{2+} ions and host framework to facilitate Zn^{2+} diffusion. It can also sustain the host framework for prolonged cycles, enhancing the rate and stable cycling performances.

3.2. $M_xV_2O_5$ (M = Na, Ca, Zn, Mg, Ag, Li …)

The above results show that water molecule intercalated into the interlayers of V_2O_5 can effectively stabilize their open-framework crystal structure to improve electrochemical performance of RZIBs. In addition, embedding large metallic ions to form the metal vanadate also is an effective method preventing structural collapse. Kundu et al. [107] synthesized single-crystal $Zn_{0.25}V_2O_5 \cdot nH_2O$ nanobelts by microwave hydrothermal technique. The results show that interlayer metal ions and structural water in this layered oxide act as pillars, enhancing structural stability and cation migration during cycling. This Zn^{2+} intercalated cathode has high specific capacities (250–300 mA h g^{-1}) and long-term cyclability (>1000 cycles) with 99% Coulombic efficiency at high current rates of 15C (1C = 300 mA g^{-1}). Xia et al. [108] proposed a double-layered calcium vanadium oxide bronze ($Ca_{0.25}V_2O_5 \cdot nH_2O$) as aqueous RZIB intercalation cathode. Compared with $Zn_{0.25}V_2O_5 \cdot nH_2O$, the nanostructure $Ca_{0.25}V_2O_5 \cdot nH_2O$ synthesized by using one-step hydrothermal method at 200 °C for 72 h offers larger CaO_7 polyhedra, smaller molecular weight and density as well as higher electrical conductivity. The $Ca_{0.25}V_2O_5 \cdot nH_2O$ cathode delivers capacities of 340 and 289 mAh g^{-1} at 0.2 and 1 C, respectively. He et al. [109] presented a low-cost, safe, high capacity (367.1 mAh g^{-1} at a current density of 0.1 A g^{-1}) and long life (with the capacity retention over 93% for 1000 cycles) aqueous RZIBs, which comprised of $Na_{0.33}V_2O_5$ nanowire cathode, 3 M $Zn(CH_3F_3SO_3)_2$ electrolyte, and zinc anode. $Na_{0.33}V_2O_5$ nanowire cathode was prepared through a simple hydrothermal method. As for the $Na_{0.33}V_2O_5$ electrode, Na^+ intercalate into $[V_4O_{12}]_n$ layers and act as "pillars" to increase the stability of the tunnel structure upon ions insertion/extraction. They have demonstrated that the intercalation of sodium ions between the $[V_4O_{12}]_n$ layers can improve electrical conductivity through single nanowire device. The result shows that the conductivity of $Na_{0.33}V_2O_5$ (5.9 × 10^4 S m^{-1}) is apparently higher than that of pure V_2O_5 (7.3 S m^{-1}). The morphology of $Na_{0.33}V_2O_5$ is well maintained after 1000 cycles and only little variety of the amount of vanadium and sodium elements are captured in the electrolyte after different cycles. Besides, the results of inductively coupled plasma optical emission spectroscopy analysis (ICP-OES) show

that the sodium content is stable at different states. In other words, the sodium ions do not change during charge/discharge process, indicating that the tunnel framework of $Na_{0.33}V_2O_5$ is maintained by Na^+ between the $[V_4O_{12}]_n$ layers, which prove the "pillars" effect of sodium ion. Fig. 5b shows the storage mechanism of zinc ion in the $Na_{0.33}V_2O_5$ electrode.

Shan et al. [110] constructed a $Zn/Ag_{0.4}V_2O_5$ system and first demonstrated the combination displacement/intercalation (CDI) reaction mechanism in aqueous RZIBs. The CDI reaction has been well-established in lithium-ion batteries, as observed in $CuTi_2S_4$ [111], $Ag_2VP_2O_8$ [112], $Ag_2VO_2PO_4$ [113], etc. The Zn^{2+}/Ag^+ displacement reaction occurs during Zn^{2+} insertion/extraction into/from the $Ag_{0.4}V_2O_5$ structure. During discharge reaction, Zn^{2+} ions insert into host material to replace the Ag^+ sites and form a new $Zn_2(V_3O_8)_2$ phase. At the same time, Ag^+ is reduced to Ag^0 to form the metallic Ag^0 network in cathode. During charge reaction, most of the Zn^{2+} ions are extracted from the electrode, and the $Zn_2(V_3O_8)_2$ is transformed back to $Ag_{0.4}V_2O_5$. In this process, small amount of Ag^0 cannot be oxidized to Ag^+, with a highly conductive Ag^0 matrix remaining within the electrode. As a result, the $Ag_{0.4}V_2O_5$ cathode performs excellent rate capability as well as long-term cycling performance (stable capacity of 144 mAh g^{-1} after 4000 cycles at 20 A g^{-1}). The CDI reaction of Zn^{2+} storage in $Ag_{0.4}V_2O_5$ provides multi-electron charge transfers and highly conductive Ag^0 matrix enables outstanding electrochemical performance (stable capacity of 144 mAh g^{-1} after 4000 cycles at 20 A g^{-1}).

They also observed the similar phenomenon upon Zn^{2+} insertion/extraction into/from the structure of copper pyrovanadate ($Cu_3(OH)_2V_2O_7\cdot2H_2O$) in 3 M $ZnSO_4$ electrolyte [114]. In this material, the inserted Zn^{2+} ions not only drive the reduction of Cu^{2+} to Cu^0 nanoparticles, but also accompany the phase transition process from $Cu_3(OH)_2V_2O_7\cdot2H_2O$ to $Zn_{0.25}V_2O_5\cdot H_2O$ (Zn^{2+} replace Cu^{2+}) upon discharge. And during the charge process, the mixed phases of $Zn_{0.25}V_2O_5\cdot H_2O$ and Cu^0 turn back to $Cu_3(OH)_2V_2O_7\cdot2H_2O$ structure upon Zn^{2+} extraction. Ming et al. [115] also found CDI reaction in layered $Mg_xV_2O_5\cdot nH_2O$ cathode. Their aqueous RZIBs system consists of $Mg_xV_2O_5\cdot nH_2O$ cathode, zinc foil anode and 3 M $Zn(CF_3SO_3)_2$ electrolyte. But different from CDI reaction in $Ag_{0.4}V_2O_5$, the deintercalated Mg^{2+} in $Mg_xV_2O_5\cdot nH_2O$ is found to deposit on Zn anode upon charge, then dissolved back in the electrolyte and served as the interaction cation along with Zn^{2+} ions upon discharge. The overall reaction can be written as:
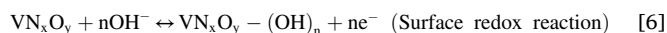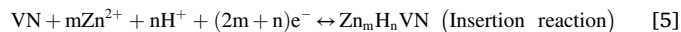
$$Zn_{0.3}Mg_xV_2O_5 + zZn \leftrightarrow Zn_{(z+0.3)}Mg_xV_2O_5 \qquad [4]$$
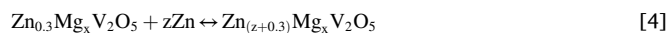
Yang et al. [116] synthesized a new $Li_xV_2O_5\cdot nH_2O$ cathode of RZIBs via a one-step hydrothermal method and followed by annealing process at 250 °C in air. The calculated result of XRD shows that the intercalation of Li^+ into the interlayer of $V_2O_5\cdot nH_2O$ further enlarges the interlayer distance of (001) face (13.77 Å), which is larger than that (001) face of $V_2O_5\cdot nH_2O$ (12.00 Å). The large interlayer spacing facilitates the Zn^{2+} diffusion effectively, leading to improved electrochemical performance. The electrode delivers stable capacity of 232 mAh g^{-1} after 500 cycles at 5 A g^{-1}. And a superior discharge capacity of 192 mAh g^{-1} after 1000th cycle can be obtained at 10 A g^{-1}. Most importantly, the electrode maintains stable capacities and voltage platforms at the current densities between 0.5 and 10 A g^{-1} under extreme conditions (high and low testing temperatures). A high capacity of 149 mAh g^{-1} is achieved after 800 cycles with the capacity retention of 96.1% at 50 °C, and there is no capacity fading up to 2800 cycles at 0 °C under current density of 10 A g^{-1}, which indicates the excellent temperature adaptability and potential practical application of $Li_xV_2O_5\cdot nH_2O$ cathode.

3.3. Other vanadium-based materials

In addition to the cathode materials mentioned above, other layered and tunnel-type vanadium-based compounds (such as

$Zn_3V_2O_7(OH)_2\cdot2H_2O$ [117], $Mo_{2.5+y}VO_{9+z}$ [118], $VO_{1.52}(OH)_{0.77}$ [119], LiV_3O_8 [120], $H_2V_3O_8$ [121], $Na_2V_6O_{16}\cdot1.63H_2O$ [122], $NaV_3O_8\cdot1.5H_2O$ [123], $K_2V_8O_{21}$ [124], $Na_5V_{12}O_{32}$ [125], etc.) have also been used as cathode materials for aqueous RZIBs because of their open-framework crystal structure and multiple oxidation states of vanadium. For example, in He's [121] work, a $H_2V_3O_8$ nanowire cathode with large interlayer spacing was synthesized through one-step hydrothermal method. This cathode was used in $Zn(CF_3SO_3)_2$ aqueous electrolyte, exhibiting the capacity of 423.8 mAh g^{-1} at 0.1 A g^{-1}, and excellent cycling stability with a capacity retention of 94.3% over 1000 cycles. In $H_2V_3O_8$ structure, V^{5+} and V^{4+} coexist with the ratio of 2:1, and the mixed valence of vanadium contributes to the improvement of electrochemical performance compared with other vanadium oxides [126]. Hu et al. [122] synthesized a highly durable $Zn/Na_2V_6O_{16}\cdot1.63H_2O$ nanowire cathode by a hydrothermal method. This cathode delivers a high specific capacity of 352 mAh g^{-1} at 50 mA g^{-1}, and exhibit a capacity retention of 90% over 6000 cycles at 5000 mA g^{-1} in aqueous $Zn(CF_3SO_3)_2$ electrolyte for aqueous RZIBs.

Fang et al. [127] designed a highly reversible surface-oxided vanadium nitride (VN_xO_y) cathode material for aqueous RZIB, which combines the insertion/extraction reaction and pseudo-capacitance-liked surface redox reaction mechanism. The energy storage of VN_xO_y cathode is not only accomplished by the typical cationic (Zn^{2+} and H^+) de-/intercalation accompanied by reversible cationic redox reaction ($V^{3+} \leftrightarrow V^{2+}$), but also provided by the release/uptake of anions (OH^-) on the VN_xO_y surface with reversible anionic ($N^{3-} \leftrightarrow N^{2-}$) redox, which are mainly responsible for the high reversibility and no structural degradation of VN_xO_y. Therefore, the electrochemical reaction mechanism of VN_xO_y electrode can be summarized as below:

$$VN + mZn^{2+} + nH^+ + (2m+n)e^- \leftrightarrow Zn_mH_nVN \ (\text{Insertion reaction}) \qquad [5]$$

$$VN_xO_y + nOH^- \leftrightarrow VN_xO_y - (OH)_n + ne^- \ (\text{Surface redox reaction}) \qquad [6]$$

Such a novel energy release/storage mechanism significantly enhances the performance of Zn/VN_xO_y system in mild aqueous $ZnSO_4$ electrolyte with an ultra-high-rate capability of 200 mA hg^{-1} at 30 A g^{-1} and superior long-term cyclic stability after 2000 cycles at 20 A g^{-1}, which demonstrates great promise for potential applications in grid-scale energy storage. The results show that the layered and tunnel-type vanadium-based cathode materials with large interlayer spacing can improve effectively electrochemical stability of aqueous RZIBs.

4. Prussian blue analogues (PBAs)

Prussian blue analogues (PBAs) have large open-framework structures and a general formula of $A_xM[M'(CN)_6]_y\cdot nH_2O$ (A = metal ions; M = Fe, Ni, Mn, V, Mo, Cu, Co; M' = Fe, Co, Cr, Ru). They belong to the Fm-3m space group with a face centered cubic structure, two metal ions (M and M′) are linked together by cyanide (CN) ligands [128]. Due to the properties of non-toxic, inexpensive, easy to synthesize and open-framework structure, PBAs have already proven to be good host materials for monovalent metal-ion batteries (Li^+, Na^+, and K^+) [129–131] as well as for multivalent metal-ion batteries (Mg^{2+}, Al^{3+} and Zn^{2+}) [132,133]. Zhang et al. [134] synthesized a rhombohedral $Zn_3[Fe(CN)_6]_2$ (ZnHCF) cathode by using high temperature co-precipitation method and explored the cycling stability of ZnHCF in different electrolytes (0.5 M Na_2SO_4, 0.5 M K_2SO_4, 1 M $ZnSO_4$). When ZnHCF cathode is subjected to be cycled in Na_2SO_4 and/or K_2SO_4 electrolytes, the color of electrolytes changes from colorlessness to light yellow, while $ZnSO_4$ electrolyte remain colorless during the cycling. The change of CV and color show the dissociation of ZnHCF in Na_2SO_4 and K_2SO_4 electrolytes to produce $[Fe(CN)_6]^{3-}$ or $[Fe(CN)_6]^{4-}$. In order to confirm the existence of $[Fe(CN)_6]^{3-}$ or $[Fe(CN)_6]^{4-}$, the electrolytes are analyzed by Ultraviolet–visible spectroscopy. There are three characteristic absorption bands of $[Fe(CN)_6]^{3-}$ at 260 nm, 302 nm and 420 nm in both
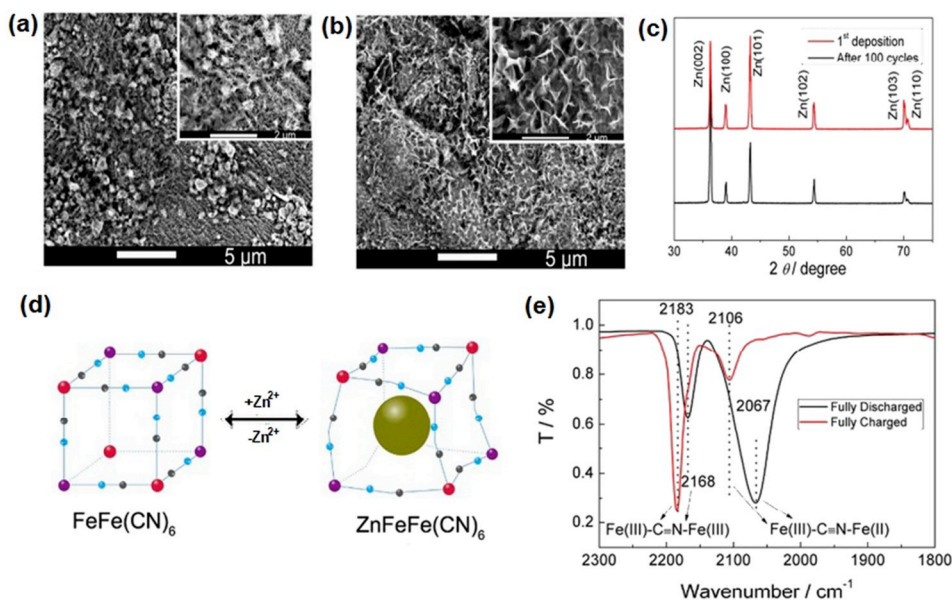
Fig. 6. (a,b) SEM images of initial Zn deposits and after 100 cycles. (c) XRD patterns of initial Zn deposits and after 100 cycles. (d) Schematic demonstration of the insertion of Zn^{2+} ions in $FeFe(CN)_6$. (e) FT-IR of fully charged and discharged $FeFe(CN)_6$. Reproduced with permission from Ref. [138]. Copyright 2016 American Chemical Society.

Na_2SO_4 and K_2SO_4 electrolytes, but no absorption bands in $ZnSO_4$ electrolytes [135]. Besides, $[Fe(CN)_6]^{3-}$ (or $[Fe(CN)_6]^{4-}$) can react with Fe^{2+} (or Fe^{3+}) ions to form insoluble (or soluble) Prussian blue $Fe_3[Fe(CN)_6]_2$ (or $KFeFe(CN)_6$). After adding $FeSO_4$ solution into three electrolytes, the colors of Na_2SO_4 and K_2SO_4 electrolytes quickly change from light yellow to blue, but $ZnSO_4$ electrolyte remains colorless. Above results show that ZnHCF undergoes dissociation upon cycling in aqueous Na_2SO_4 and K_2SO_4 electrolytes, but is quite stable in aqueous $ZnSO_4$ electrolyte.

Mantia et al. [136] synthesized a copper hexacyanoferrate (CuHCF) nanopowder cathode by a co-precipitation method. This CuHCF cathode

in the $ZnSO_4$ electrolyte yields an average voltage of 1.73 V. But $ZnSO_4$ electrolyte has hydrogen evolution near the surface of the zinc electrode and the formation of zinc oxide, which block the surface and subsequently decrease Zn^{2+} ions diffusion. To avoid these intrinsic problems, Hong et al. [137] synthesized $K_{0.86}Ni[Fe(CN)_6]_{0.954}(H_2O)_{0.766}$ nanoparticles by a simple precipitation method and studied the electrochemical performances of RZIB using $K_{0.86}Ni[Fe(CN)_6]_{0.954}(H_2O)_{0.766}$ as cathode and zinc metal as anode in an organic electrolyte (acetonitrile (AN) contained 0.5 M $Zn(ClO_4)_2$). This battery exhibits an excellent reversible discharge capacity of 55.6 mAh g^{-1} and a discharge voltage of 1.19 V (vs. Zn^{2+}/Zn) at a rate of 0.2 C. The results show that the organic
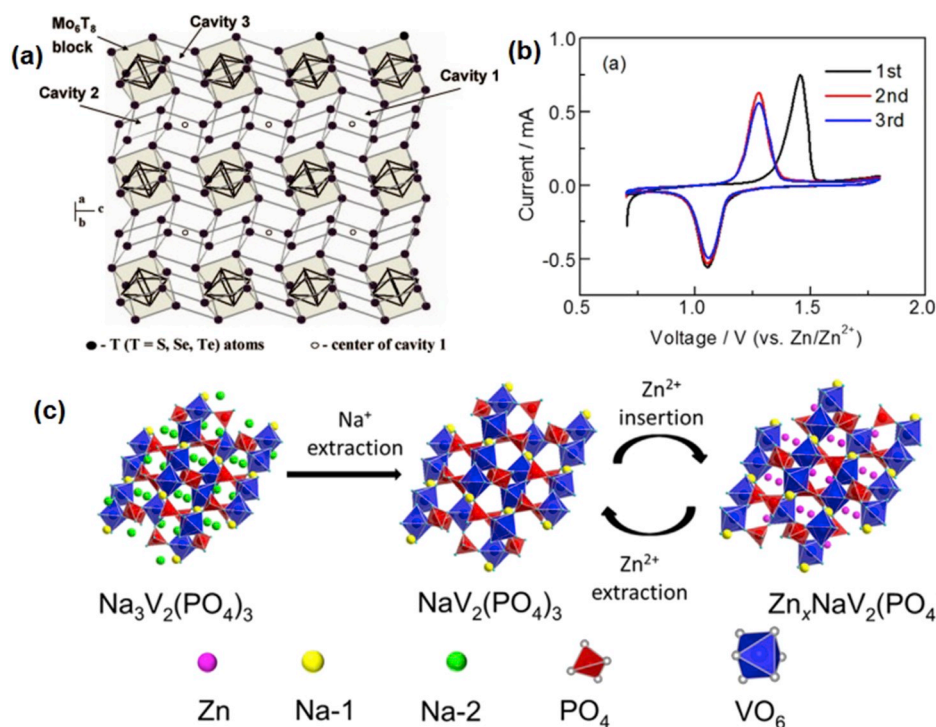
Fig. 7. (a) Basic Chevrel phases' crystal structure: three types of cavities between Mo_6S_8 blocks. The face-sharing pseudocubes of cavities 1 and 2 form the channels in direction c (one of three equivalent directions in rhombohedral crystals). Reproduced with permission from Ref. [140]. Copyright 2009 American Chemical Society. (b) Cyclic voltammogram behaviors of $Na_3V_2(PO_4)_3/Zn$ at a scan rate of 0.1 mV s^{-1}. (c) Schematic representation for phase transition of $Na_3V_2(PO_4)_3$ cathode during cycling. Reproduced with permission from Ref. [151]. Copyright 2016 Elsevier Ltd.

electrolyte system also provides a high zinc cycling efficiency (>99.9%) than the aqueous system (~80%), but the formation of dendritic zinc seems to be unavoidable after cycles in this organic electrolyte.

Developing biodegradable and biocompatible ionic liquid is an alternative strategy to overcome these drawbacks of organic electrolyte, such as dendritic zinc and eco-toxicity Liu et al. [138] prepared FeFe (CN)$_6$ nanoparticle cathode by a solution precipitation method and designed a FeFe(CN)$_6$/zinc RZIB with a cheap and green bio-ionic liquid-water mixture electrolyte contained choline acetate of 30 wt%. The electrochemical cycling behavior of the Zn anode was investigated by using scanning electron microscopy (SEM) and XRD (Fig. 6a–c). By comparing SEM images (Fig. 6a and b) of initial Zn deposits and after 100 cycles, there are some very minor changes in morphology, which shows that the Zn anode has high stability in this electrolyte during the cycling. XRD results of the Zn anodes in Fig. 6c show only the diffraction peaks of Zn even after 100 charge/discharge cycles, further indicating the high stability of the Zn anode in bio-ionic liquid-water mixtures. They also studied electrochemical insertion and extraction of Zn^{2+} ions in FeFe(CN)$_6$ cathode. The schematic demonstration of the insertion of Zn^{2+} ions in FeFe(CN)$_6$ is shown in Fig. 6d. According to the result of Fourier Transform infrared spectroscopy (FT-IR) (Fig. 6e), there are peaks at 2183 and 2106 cm^{-1} in fully charged cathode (red curve), which attribute to the cyanide stretching vibration mode, ν(CN) of Fe (III)Fe(III)(CN)$_6$ and Fe(III)Fe(II)(CN)$_6$ [139]. In the discharged state (black curve), these peaks shift to a lower wavenumber of 2168 and 2067 cm^{-1} and change their relative intensities, indicating that Zn^{2+} ions insert into FeFe(CN)$_6$ and Fe(III) is reduced to Fe(II). The insertion of Zn^{2+} ions in PBAs is also confirmed by Energy-Dispersive X-ray spectroscopy (EDX), the result shows a Fe to Zn molar ratio of ~3:1 in fully discharged FeFe(CN)$_6$, further proves the insertion of Zn^{2+} ions in cathode material.

5. Chevrel phase

Chevrel phase M$_x$Mo$_6$T$_8$ (M = metal, T = S, Se, or Te) also is a promising material for RZIBs because of its unique crystal structure. Fig. 7a shows a basic crystal structure of Chevrel phase: three types of cavities between Mo$_6$S$_8$ blocks (or Mo$_6$-octahedral clusters inside anion cubes). The face-sharing pseudocubes of cavities 1 and 2 form the open three-dimensional channels in direction c (one of three equivalent directions in rhombohedral crystals). Cavities 1 and 2 are available for cations insertion but cavity 3 not allows the occupation due to the strong repulsion between Mo atoms and inserting cations [140,141]. Chevrel phase compounds can accommodate various cations, such as monovalent (Li$^+$, Na$^+$) as well as divalent (Zn^{2+}, Cd^{2+}, Co^{2+}, Mg^{2+}) at ambient temperatures and have outstanding capability [142–144].

Chae et al. [145] researched the properties of the Zn$_x$Mo$_6$S$_8$ (x = 1, 2) Chevrel phases, which prepared by electrochemical insertion of Zn^{2+} ions into Mo$_6$S$_8$. The Mo$_6$S$_8$ was first prepared via the chemical extraction of Cu ions from Cu$_2$Mo$_6$S$_8$ synthesized via a solid-state reaction for 24 h at 1000 °C. They find that the processes of Zn^{2+} ions insertion into Mo$_6$S$_8$ in different potential regions involve two steps. The first step occurs at higher-voltage region (around 0.45–0.50 V in CV) corresponding to the formation of ZnMo$_6$S$_8$ from Mo$_6$S$_8$. The second step occurs at a potential of around 0.35 V in CV, which defines the further reduction to form Zn$_2$Mo$_6$S$_8$ from ZnMo$_6$S$_8$. Cheng et al. [146] synthesized Chevrel phase Mo$_6$S$_8$ nanocubes through an intermediate compound of Cu$_2$Mo$_6$S$_8$, and acid leaching of Cu^{2+} ions and applied as the electrode material for RZIB. The sizes of Mo$_6$S$_8$ range from 20 to 150 nm with an average size of ~100 nm. This Mo$_6$S$_8$ host can host Zn^{2+} ions reversibly in both aqueous and nonaqueous electrolytes with specific capacities around 90 mAh g^{-1}, and exhibits remarkable intercalation kinetics and cyclic stability.

6. Polyanionic materials

NASICON-typed polyanionic materials possess extremely stable framework structure, large channel and plenty of vacancies, which can be used as Zn^{2+} ions storage guests for improving ionic diffusion capability and long cycle stability [147,148]. NASICON-typed Na$_3$V$_2$(PO$_4$)$_3$ (NVP) as host material for Na$^+$ ions have been widely studied [149,150]. Huang et al. [151] obtained NVP nanoparticles by hydrothermal route followed by post calcination and first applied as intercalation host for divalent cations. They developed a new and eco-friendly RZIB by using NVP as cathode, zinc as anode and Zn(CH$_3$COOH)$_2$ as aqueous electrolyte. This aqueous battery delivers a reversible capacity of 97 mAh g^{-1} at 0.5 C and retains 74% capacity after 100 cycles. Meanwhile, the battery can be charged and discharged at high rate up to 10 C and the specific discharge capacity is 58 mAh g^{-1}. Fig. 7b is CV behaviors of this system at a scan rate of 0.1 mV s^{-1}. The oxidation peak in the first cycle at about 1.46 V vs. Zn^{2+}/Zn corresponds to Na$^+$ ions deintercalation from NVP. The redox pair peaks during subsequent cycles appear at about 1.05 and 1.28 V, which can be attributed to Zn^{2+} ions deintercalate/intercalate from/into NVP cathode. As for the intercalation mechanisms of Zn^{2+} ions, they proposed that the NVP phase transform to NaV$_2$(PO$_4$)$_3$ during charging accompany by the oxidation from V^{3+} to V^{4+}. When discharging, Zn^{2+} ions insert into the NaV$_2$(PO$_4$)$_3$ framework to form new Zn$_x$NaV$_2$(PO$_4$)$_3$ phase and V^{4+} is reduced back to V^{3+}. After recharging, V^{3+} is oxidized to V^{4+} accompanied by extraction of Zn^{2+} ions. The phase transition of Na$_3$V$_2$(PO$_4$)$_3$ cathode during cycling is shown in Fig. 7c.

Na$_3$V$_2$(PO$_4$)$_2$F$_3$ (NVPF) is another NASICON-typed cathode material and presents more stable structure than NVP because of the strong affinity of F atoms toward the surroundings [152,153]. Li et al. [30] first reported NVPF as a Zn intercalation cathode in 2 M Zn(CF$_3$SO$_3$)$_2$ electrolyte for RZIB. The Zn storage mechanism is similar to NVP cathode, NVPF is initially converted into Na$_2$V$_2$(PO$_4$)$_2$F$_3$, and then 0.5 Zn^{2+} ions are inserted into Na$_2$V$_2$(PO$_4$)$_2$F$_3$ to form Zn$_{0.5}$Na$_2$V$_2$(PO$_4$)$_2$F$_3$, after which Zn^{2+} ions are reversibly shuttled back and forth between Zn$_{0.5}$Na$_2$V$_2$(PO$_4$)$_2$F$_3$ and Na$_2$V$_2$(PO$_4$)$_2$F$_3$. Interestingly, they fabricate a carbon film functionalizing Zn anode by rolled 80 wt% carbon black (super P) and 20 wt% PTFE into thin carbon film (thickness, ~0.1 mm) and placed on the surface of a Zn foil. The carbon film can change the deposition behavior of Zn and inhibit the dendritic Zn growth. There are large pieces of Zn dendrites perpendicularly grow and accumulate on the surface of Zn foil after 200 cycles (400 h). While much small and relatively homogeneous distribution of Zn plates tend to parallel growth on the surface of Zn anode with carbon film. Due to the stable structure of NVPF and carbon film functionalizing Zn anode, this RZIB exhibits a high voltage of 1.62 V and remarkable cyclability of 95% capacity retention over 4000 cycles at 1 A g^{-1}.

7. Metal disulfides

Layered metal disulfides, such as VS$_2$ [154] and MoS$_2$ [155], have attracted tremendous attention as electrode materials for energy storage and conversion. The unique layered structure bonded by weak van der Waals' forces in these materials promotes the mass transport of various charge carriers and can also accommodate the volume variations during intercalation of ions. He et al. [156] synthesized VS$_2$ nanosheets by hydrothermal route and used VS$_2$ nanosheets as cathode for aqueous RZIB. VS$_2$ belongs to hexagonal system and the interlayer spacing is 5.76 Å. Their results demonstrate that the interlayer space of VS$_2$ can self-adapt to the intercalation of Zn^{2+} with an expansion along the c-axis (only 1.73%) and a slightly shrink along the a- and b-axes. Insertion of Zn^{2+} ions into the interlamination of VS$_2$ layer during the discharge can be divided into two steps. First, the phase change from VS$_2$ to conductive Zn$_{0.09}$VS$_2$ occurs in the voltage range of 0.82–0.65 V, and the subsequent phase transition from Zn$_{0.09}$VS$_2$ to Zn$_{0.23}$VS$_2$ occurs in the voltage range of 0.65–0.45 V. In charging process, Zn^{2+} ions deintercalate from
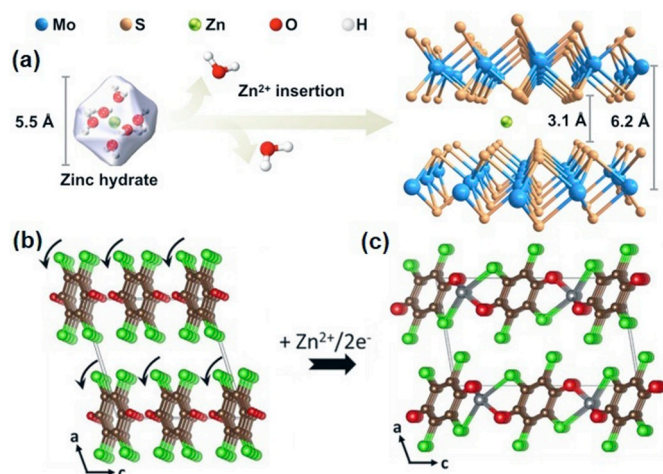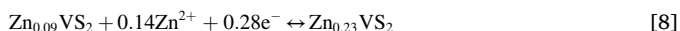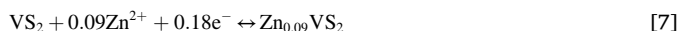
Fig. 8. (a) Schematic illustration of Zn^{2+} insert into pristine MoS_2. Reproduced with permission from Ref. [157]. Copyright 2019 American Chemical Society. (b) Structural models of *p*-chloranil and (c) Zn-*p*-chloranil ($Zn \cdot C_6Cl_4O_2$) as obtained from density functional theory (DFT) structural optimization. The curved arrows in (b) show the direction of the rotation of the pchloranil molecular columns upon Zn^{2+} insertion. Color code: C (brown), Cl (green), O (red), and Zn (gray). Reproduced with permission from Ref. [165]. Copyright 2018 American Chemical Society. (For interpretation of the references to color in this figure legend, the reader is referred to the Web version of this article.)

$Zn_{0.23}VS_2$ and gradually change back to VS_2 phase. The electrochemical reaction in the VS_2 cathode can be summarized as below:

$$VS_2 + 0.09Zn^{2+} + 0.18e^- \leftrightarrow Zn_{0.09}VS_2 \qquad [7]$$

$$Zn_{0.09}VS_2 + 0.14Zn^{2+} + 0.28e^- \leftrightarrow Zn_{0.23}VS_2 \qquad [8]$$

MoS_2 can reversibly intercalate Li^+ and Na^+ ions but does not readily intercalate Zn^{2+} ions with higher valence. Liang et al. [157] realized fast Zn^{2+} diffusion in MoS_2 through simple interlayer spacing and hydrophilicity engineering which achieved by oxygen incorporation (MoS_2–O). The smaller size of O atoms (48 p.m. vs 88 p.m. of S atoms) and the shorter Mo–O bonds (1.86 Å vs 2.42 Å of Mo–S bonds) weaken the van der Waals interactions between the two adjacent S layers, therefore resulting in the interlayer spacing to increase from 6 to 9 Å. In addition, the oxygen incorporation improves the hydrophilicity, lowers the Zn^{2+} intercalation energy. The schematic demonstration of the insertion of Zn^{2+} ions in pristine MoS_2 is shown in Fig. 8a. In 3 M Zn $(CF_3SO_3)_2$ electrolyte, the RZIB based on MoS_2–O cathode delivers a discharge capacity of 232 mAh g^{-1} at 0.1 A g^{-1}, which is much higher than that of MoS_2 based RZIB (21 mAh g^{-1}). More importantly, the Zn^{2+} diffusivity in MoS_2–O is boosted by 3 orders of magnitude compared with unmodified MoS_2. Xu et al. [158] prepared the defect-rich MoS_{2-x} nanosheets by a simple hydrothermal process followed by heat treatment and applied defect engineering to enhance the electrochemical activity of MoS_2 electrode. These MoS_{2-x} nanosheets show a preferential insertion of Zn ions into sulfur vacancies, allowing a much greater capacity to be obtained compared to pure MoS_2. The electrochemical reaction in MoS_{2-x} cathode can be written as follows:

$$MoS_{2-X} + 0.36Zn^{2+} + 0.728e^- \leftrightarrow Zn_{0.36}MoS_{2-X} \qquad [9]$$
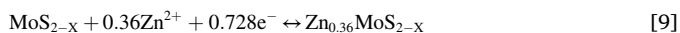
The phase transition from MoS_{2-x} to $Zn_{0.36}MoS_{2-x}$ occurs in the discharge process, and Zn^{2+} ions extract from $Zn_{0.36}MoS_{2-x}$ to form the MoS_{2-x} phase gradually during charging process. This defect-rich MoS_{2-x} electrode provides a high reversible capacity of 135 mAh g^{-1} at 100 mA g^{-1}. Moreover, the MoS_{2-x} can deliver a high reversible capacity of 88.6 mAh g^{-1} with capacity retention of 87.8% at 1000 mA g^{-1} after 1000 cycles. The defect-rich MoS_{2-x} cathode displays excellent electrochemical performance, making it a highly promising cathode material

for application in RZIBs.

8. Organic materials

Organic cathode materials also are very attractive for RZIBs because of its unique advantages, such as flexible synthesis, lightweight, low cost, abundant resource and benign to the environment [159]. Some organic quinone compounds have offered an interesting alternative to inorganic cathode materials for nonaqueous lithium and sodium ion batteries, but those batteries suffer fast capacity fading due to the dissolution of active materials in organic electrolytes [160]. Applying quinone electrodes in aqueous batteries makes it possible to achieve stable electrochemical performance because quinones are barely soluble in aqueous electrolytes [161,162]. Zhao et al. [163] reported an aqueous RZIB with organic calix [4]quinone (C4Q) cathode, Zn foil anode and 3 M $Zn(CF_3SO_3)_2$ electrolyte. The C4Q cathode with open bowl structure and eight carbonyls was synthesized by using calix [4]arene as a precursor and green *p*-aminobenzoic acid as a major component of folic acid [164]. The active centers of C4Q cathode are carbonyls (C=O double bond) in para-position, but the ortho carbonyls in C4Q cathode would cause larger steric hindrance for Zn^{2+} ions reactions, thus showing poor electrochemical performance. They also investigated the electrochemical performance distinction of C4Q cathode between filter paper separator and cation-selective membrane (Nafion) separator. The result reveals that the batteries with the Nafion membrane show higher stable cycling performance (93% capacity retention after 100 cycles). The uptake of Zn^{2+} ions will ionize the C4Q to form ZnxC4Q during discharging. Then, the dissociation of Zn_xC4Q to Zn^{2+} and $C4Q^{2x-}$ makes it more soluble than C4Q. The dissolved $C4Q^{2x-}$ in electrolyte can pass through the filter paper and react with zinc forming a by-product on the anode side, which causes the decline of capacity. Therefore, the batteries with the Nafion membrane show higher stable cycling performance because of the prevention of anions from crossing.

Kundu et al. [165] presented another tetrachloro-1,4-benzoquinone (*p*-chloranil) organic cathode for aqueous RZIB. This *p*-chloranil material hold together by weak intermolecular van der Waals force, posing only a modest Coulomb repulsion to the diffusing cations, which is facile and reversible for the intercalation of hard divalent cations. Fig. 8b and c shows the fully relaxed structure of pure *p*-chloranil and Zn^{2+} inserted *p*-chloranil, respectively. Interestingly, malleable lattice of *p*-chloranil allows a squeezing reorientation to make pathways for incoming Zn^{2+} by increasing the O–O distance and decreasing the Cl–Cl distance, which driven by the insertion of Zn^{2+} ions. In other words, the reorientation can be called as the rotation of stacked chloranil columns. The coordination of Zn^{2+} with two O and Cl of two chloranil molecules of adjacent columns produces atomic distances change, resulting in the accommodation of Zn^{2+} ions in a slightly distorted tetrahedral environment. The structural flexibility facilitates a high capacity of $\geq$200 mAh g^{-1} with a very small voltage polarization of 50 mV in a flat plateau around 1.1 V.

Porous crystalline covalent organic frameworks (COFs) have been widely explored as host materials for monovalent ions (H^+, Li^+, Na^+) in energy storage system due to its structural tunability, well-defined porosity, and high chemical stability. Kurungot et al. [166] first demonstrated hydroquinone (HqTp) based COF acting as cathode material for aqueous RZIB. The C=O and N–H functionalities in polymers are capable of coordinating Zn^{2+} ions in electrochemical system. Besides, HqTp possesses crystalline honey-comb structure with a unique pore size of 1.5 nm, which further boosts the movement of Zn^{2+} ions through the entire organic cathode. In their works, the efficient inter-layer interaction of divalent Zn^{2+} ions with C=O (O···Zn, ~2.0 Å) and N–H (N···Zn, ~2.0 Å) from the adjacent layers provides an excellent discharge capacity of 276 mAh g^{-1} at 125 mAg^{-1} in an operating potential of 0.2–1.6 V vs Zn/Zn^{2+}. Wang et al. [167] first applied 1,4,5, 8-naphthalene diimide (NTCDI) as cathode material for aqueous RZIB. The highly activated NTCDI is synthesized by dissolving 1,4,5,8-naphthalenetetracarboxylic dianhydride (NTCDA) in ammonia solution to

Table 4
Synthesis methods and synthesis conditions of various cathode materials with different structures.

Cathode material	Synthesis method	Temperature	Time	Sintering	Ref.
α-MnO$_2$ nanorod	Microemulsion method			no	[42]
α-MnO$_2$ nanorod	Microemulsion method			no	[44]
α-MnO$_2$ nanorod	Hydrothermal method	140 °C	24 h	no	[48]
α-MnO$_2$ nanorod	Hydrothermal method	140 °C	24 h	no	[51]
α-MnO$_2$ nanorod	Hydrothermal method	140 °C	24 h	no	[56]
α-MnO$_2$ nanofibre	Hydrothermal method	120 °C	12 h	no	[62]
α-MnO$_2$ nanowire	Hydrothermal method	120 °C	12 h	no	[92]
β-MnO$_2$ nanorod	Microwave-assisted hydrothermal method	200 °C	10min	no	[65]
β-MnO$_2$ nanorod	Hydrothermal method	140 °C	12 h	no	[66]
γ-MnO$_2$ nanowire	Redox reaction process			200 °C/24 h	[70]
ε-MnO$_2$@CFP (Carbon fiber paper)	Electrodeposition method			no	[72]
δ-MnO$_2$ nanoflake	Thermal decomposition method	350 °C	5 h	no	[73]
Todorokite MnO$_2$ nanorod	Hydrothermal method	160 °C	24 h	no	[80]
Spinel ZnMn$_2$O$_4$ microsphere	Solvothermal method	180 °C	12 h	600 °C/4 h	[90]
MnO$_2$ nanorod/CNT (Carbon nanotube)	Co-precipitation method			no	[94]
V$_2$O$_5$ microplate	Hydrothermal method	180 °C	12 h	350 °C/2 h	[98]
V$_2$O$_5$/CFS (Carbon foam substrate)	Electrodeposition method			no	[102]
Zn$_{0.25}$V$_2$O$_5$·nH$_2$O nanobelt	Microwave-assisted hydrothermal method	180 °C	90min	no	[107]
Ca$_{0.25}$V$_2$O$_5$·nH$_2$O nanobelt	Hydrothermal method	200 °C	72 h	no	[108]
Na$_{0.33}$V$_2$O$_5$ nanowire	Hydrothermal method	180 °C	48 h	no	[109]
Ag$_{0.4}$V$_2$O$_5$ nanobelt	Hydrothermal method	200 °C	48 h	no	[110]
Cu$_3$(OH)$_2$V$_2$O$_7$·2H$_2$O nanosheet	Hydrothermal method	200 °C	48 h	no	[114]
Mg$_x$V$_2$O$_5$·nH$_2$O nanobelt	Hydrothermal method	220 °C	48 h	no	[115]
Li$_x$V$_2$O$_5$·nH$_2$O nanosheet	Hydrothermal method	200 °C	48 h	250 °C/2 h	[116]
H$_2$V$_3$O$_8$ nanowire	Hydrothermal method	180 °C	60 h	no	[121]
Na$_2$V$_6$O$_{16}$·1.63H$_2$O nanowire	Hydrothermal method	180 °C	24 h	400 °C/3	[122]
Zn$_3$[Fe(CN)$_6$]$_2$ particle	Co-precipitation method			no	[134]
CuHCF nanopowder	Co-precipitation method			no	[136]
K$_{0.86}$Ni[Fe(CN)$_6$]$_{0.954}$(H$_2$O)$_{0.766}$ nanoparticle	Co-precipitation method			no	[137]
FeFe(CN)$_6$ nanoparticle	Co-precipitation method			no	[138]
Zn$_x$Mo$_6$S$_8$ particle	solid-state reaction			1000 °C/24 h	[145]
Mo$_6$S$_8$ nanoparticle	solid-state reaction			1000 °C/7 h	[146]
Na$_3$V$_2$(PO$_4$)$_3$ nanoparticle	Hydrothermal method	180 °C	48 h	350 °C/5 h 750 °C/8 h	[151]
Na$_3$V$_2$(PO$_4$)$_2$F$_3$ particle	sol-gel method			650 °C/8 h	[30]
VS$_2$ nanosheet	Hydrothermal method	180 °C	20 h	no	[156]
MoS$_2$ nanosheet	Hydrothermal method	180 °C	24 h	no	[157]
MoS$_2$ nanosheet	Hydrothermal method	200 °C	18 h	250 °C/2 h	[158]
MoS$_2$ nanosheet	Hydrothermal method	190 °C	24 h	no	[173]
Layered ribbon-like hydroquinone (HqTp)	solid-state mechano-mixing			no	[166]

replacing the O in C–O–C bonds with N. Nitrogen substitution can improve the poor electrochemical performance of NTCDA. In 2 M ZnSO$_4$ aqueous electrolyte, the RZIB based on NTCDI cathode and Zn anode presents a high reversible capacity of 240 mAh g^{-1} at 0.1 A g^{-1} and capacity retention of 73.7% after 2000 cycles at 1 A g^{-1}. The structural regulation strategy in NTCDI creates a new chance for designing cathode material for zinc storage.

9. Conclusions and future outlook

Plenty of investigations show that rechargeable zinc-ion batteries (RZIBs) are one of the most promising energy storage systems to replace lithium-ion batteries. The charge storage mechanism of RZIBs is established on the migration of Zn^{2+} ions between cathode and anode materials. The cathode material is the most critical component of RZIBs, determining the performance of whole RZIBs. Although cathode materials have progressed in recent years, there are still significant challenges to overcome before reaching large-scale commercialization. In this review, the synthesis, composition, structure and electrochemical properties of various cathode materials of RZIBs have been summarize, which include manganese-based oxide, vanadium-based materials, Prussian blue analogues, Chevrel phases, polyanionic compounds, metal disulfides and organic compounds. Manganese-based dioxides have been widely used as cathode materials of RZIBs because of high electrochemically active, environmentally friendly and relatively cheap. Manganese-oxide cathode materials include α-, β-, γ-, ε-, δ-, todorokite-MnO$_2$ with different tunnel features and spinel ZnMn$_2$O$_4$. At present, three energy storage mechanism of manganese-based dioxide cathode

materials have been proposed: (1) the reversible insertion/extraction of zinc ions into/from MnO$_2$; (2) Zn^{2+} was deposited on the surface of MnO$_2$ and formed zinc hydroxide sulfate (Zn$_4$(OH)$_6$(SO$_4$)·5H$_2$O); and (3) reversible Zn^{2+}/H$^+$ co-insertion/extraction mechanism. Although manganese-based oxide materials have been explored widely, its reversible phase transition during charge/discharge process easily leads to an excessive structural stress, resulting in the formation of amorphous phase and decay of capacity.

Vanadium-based cathode materials have also been developed because of its open-framework crystal structure, multiple oxidation states of vanadium and simple zinc ion insertion/extraction reaction mechanism. Compared with manganese-based materials, the vanadium-based cathode materials improved effectively the cycle stability and rate performance of RZIBs because interlayer metal ions (Na, Ca, Zn, Mg, Ag, Li …) in the layered structure act as pillars to minimize the steric hindrance, but have lower voltage platform. Prussian blue analogue cathodes have large open-framework structures, their low capacity (~50 mAh g^{-1}) and O$_2$ evolution at high voltage (~1.7 V vs. Zn^{2+}/Zn) hinder their further application. Currently, the researches on Chevrel phases, polyanionic compounds and organic quinone compounds have just started and the relevant reports are few, and their capacity and rate performance need to be further improved. In brief, the development of the RZIBs is still in the primary stage, which requires increasing research efforts to achieve industrialization, especially in terms of cathode materials.

In synthesis of cathode materials of RZIBs, the synthesis methods and synthesis conditions often play a crucial role in deciding the particle size, crystallinity, morphology, structure and electrochemical

Table 5

Electrochemical performances of RZIBs based on various cathodes and electrolytes.

Cathode material	Cathode composition	Electrolyte	Average discharge voltage(V)	Discharge capacity	Cycle performance
α-MnO$_2$ [42]	MnO$_2$: carbon black: PVDF = 7:2:1	1 M ZnSO$_4$ or Zn(NO$_3$)$_2$	1.40	210 mAh g^{-1} at 0.5C	100% retained after 100 cycles at 6C
α-MnO$_2$ [48]	MnO$_2$: carbon black: PVDF = 7:1:2	1 M ZnSO$_4$	1.30	194 mAh g^{-1} at C/20	65% retained after 30 cycles at C/20
α-MnO$_2$ [51]	MnO$_2$: carbon black: PVDF = 7:1:2	1 M ZnSO$_4$	1.25	167 mAh g^{-1} at C/5	70% retained after 30 cycles at C/5
α-MnO$_2$ [62]	MnO$_2$: carbon black: PVDF = 7:2:1	2 M ZnSO$_4$ + 0.1 M MnSO$_4$	1.35&1.25	285 mAh g^{-1} at C/3	92% retained after 5000 cycles at 5C
α-MnO$_2$ [94]	MnO$_2$: carbon black: LA133 water based adhesives: CMC = 7:2:0.8:0.2	2 M ZnSO$_4$ + 0.5 M MnSO$_4$	1.60&1.38	665 mAh g^{-1} at 100 mA g^{-1}	99% retained after 500 cycles at 5000 mA g^{-1}
α-MnO$_2$ [92]	MnO$_2$: Super-P: PTFE = 7:2:1	2 M ZnSO$_4$ + 0.2 M MnSO$_4$	1.25&1.38	382 mAh g^{-1} at 300 mA g^{-1}	94% retained after 3000 cycles at 3000 mA g^{-1}
β-MnO$_2$ [65]	MnO$_2$: Super-P: CMC = 8:1:1	1 M ZnSO$_4$+ 0.1 M MnSO$_4$	1.60&1.25	270 mAh g^{-1} at 100 mA g^{-1}	75% retained after 200 cycles at 200 mA g^{-1}
γ-MnO$_2$ [70]	MnO$_2$: Ketjen black: TAB = 7:2:1	1 M ZnSO$_4$	1.30&1.20	285 mAh g^{-1} at 0.05 mA cm^{-2}	63% retained after 40 cycles at 0.5 mA cm^{-2}
ε-MnO$_2$ [72]	MnO$_2$+CFP (carbon fiber paper)	2 M ZnSO$_4$ + 0.2 M MnSO$_4$	1.40&1.30	260 mAh g^{-1} at 1.3C	99% retained after 10000 cycles at 6.5 C
δ-MnO$_2$ [73]	MnO$_2$: Ketjen black: TAB = 7:2:1	1 M ZnSO$_4$	1.38&1.23	250 mAh g^{-1} at 83 mA g^{-1}	46% retained after 100 cycles at 83 mA g^{-1}
δ-MnO$_2$ [74]	MnO$_2$	0.5 M Zn(TFSI)$_2$ in acetonitrile	1.25	123 mAh g^{-1} at 12.3 mA g^{-1}	48% retained after 125 cycles at 12.3 mA g^{-1}
Todorokite MnO$_2$ [80]	MnO$_2$: carbon black: PVDF = 8.5:1:0.5	1 M ZnSO$_4$	1.70&1.25	108 mAh g^{-1} at C/2	83% retained after 50 cycles at C/2
Spinel ZnMn$_2$O$_4$ [86]	ZnMn$_2$O$_4$: PVDF = 9:1	3 M Zn(CF$_3$SO$_3$)$_2$	1.35&1.10	150 mAh g^{-1} at 50 mA g^{-1}	94% retained after 500 cycles at 500 mA g^{-1}
Spinel ZnMn$_2$O$_4$ [90]	MnO$_2$: acetylene black: PVDF = 8:1:1	1 M ZnSO$_4$ + 0.05 M MnSO$_4$	1.35&1.20	70.2 mAh g^{-1} at 3000 mA g^{-1}	106.5 mAh g^{-1} after 300 cycles at 100 mA g^{-1}
V$_2$O$_5$ [97]	V$_2$O$_5$	3 M ZnSO$_4$	1.10&0.70	224 mAh g^{-1} at 100 mA g^{-1}	44% retained after 100 cycles at 500 mA g^{-1}
V$_2$O$_5$ [98]	V$_2$O$_5$: acetylene black: PVDF = 7:2:1	1 M Zn(CF$_3$SO$_3$)$_2$ + 21 M LiTFSI	1.10&0.90	238 mAh g^{-1} at 50 mA g^{-1}	80% retained after 2000 cycles at 2000 mA g^{-1}
V$_2$O$_5$ [102]	V$_2$O$_5$	0.5 M Zn(TFSI)$_2$ in acetonitrile	~0.80	196 mAh g^{-1} at C/10	87% retained after 120 cycles at C/10
V$_2$O$_5$·nH$_2$O [105]	V$_2$O$_5$: Super-P: PVDF = 7:2:1	3 M Zn(CF$_3$SO$_3$)$_2$	0.91&0.54	381 mAh g^{-1} at 60 mA g^{-1}	71% retained after 900 cycles at 6000 mA g^{-1}
Zn$_{0.25}$V$_2$O$_5$·nH$_2$O [107]	Zn$_{0.25}$V$_2$O$_5$: Super-P: CMC:SBR = 7:2.7:0.2:0.1	1 M ZnSO$_4$	~0.9	282 mAh g^{-1} at 300 mA g^{-1}	81% retained after 1000 cycles at 2400 mA g^{-1}
Ca$_{0.25}$V$_2$O$_5$·nH$_2$O [108]	Ca$_{0.25}$V$_2$O$_5$: Super-P: CMC:SBR = 7:2.7:0.2:0.1	1 M ZnSO$_4$	0.75&1.15&1.33	289 mAh g^{-1} at 1C	96% retained after 3000 cycles at 80C
Na$_{0.33}$V$_2$O$_5$ [109]	Na$_{0.33}$V$_2$O$_5$: Super-P: PVDF = 7:2:1	3 M Zn(CF$_3$SO$_3$)$_2$	1.10&0.79, 0.63& 0.52	367.1 mAh g^{-1} at 100 mA g^{-1}	93% retained after 1000 cycles at 200 mA g^{-1}
Mg$_x$V$_2$O$_5$·nH$_2$O [115]	Mg$_x$V$_2$O$_5$: single wall carbon nanotubes: CMC: SBR = 7:2.7:0.2:0.1	3 M Zn(CF$_3$SO$_3$)$_2$	0.50&0.70		
0.90&1.30	353 mAh g^{-1} at 50 mA g^{-1}	97% retained after 2000 cycles at 5000 mA g^{-1}			
Li$_x$V$_2$O$_5$·nH$_2$O [116]	Li$_x$V$_2$O$_5$: acetylene black: PVDF = 7:2:1	2 M ZnSO$_4$	0.96&0.82&0.59	407.6 mAh g^{-1} at 1000 mA g^{-1}	76% retained after 500 cycles at 5000 mA g^{-1}
H$_2$V$_3$O$_8$ [121]	H$_2$V$_3$O$_8$: acetylene black: PVDF = 7:2:1	3 M Zn(CF$_3$SO$_3$)$_2$	0.49&0.73	423.8 mAh g^{-1} at 100 mA g^{-1}	94% retained after 1000 cycles at 5000 mA g^{-1}
Na$_2$V$_6$O$_{16}$ [122]	Na$_2$V$_6$O$_{16}$: acetylene black: PVDF = 7:2:1	3 M Zn(CF$_3$SO$_3$)$_2$	0.78&0.46	352 mAh g^{-1} at 50 mA g^{-1}	90% retained after 6000 cycles at 5000 mA g^{-1}
ZnHCF [134]	ZnHCF: Super-P: PVDF: KS6 = 7.5:1.2:1:0.3	1 M ZnSO$_4$	1.70	60.4 mAh g^{-1} at 120 mA g^{-1}	76% retained after 100 cycles at 300 mA g^{-1}
CuHCF [136]	CuHCF: Super-P: PVDF: SFG6 = 8:0.9:0.9:0.2	0.02 M ZnSO$_4$	1.70	53 mAh g^{-1} at 60 mA g^{-1}	96% retained after 100 cycles at 60 mA g^{-1}
K$_{0.86}$Ni[Fe (CN)$_6$]$_{0.954}$(H$_2$O)$_{0.766}$ [137]	K$_{0.86}$Ni[Fe(CN)$_6$]$_{0.954}$(H$_2$O)$_{0.766}$: Super-P: PVDF = 7:2:1	0.5 M Zn(ClO$_4$)$_2$ in acetonitrile	1.19	26.8 mAh g^{-1} at 56 mA g^{-1}	96% retained after 35 cycles at 56 mA g^{-1}
FeFe(CN)$_6$ [138]	FeFe(CN)$_6$: amorphous carbon: PVDF: SFG6 = 8:1:0.8:0.2	1 M Zn(OAc)$_2$ in [Ch] OAc + water	1.10	120 mAh g^{-1} at 10 mA g^{-1}	95% retained after 10 cycles at 10 mA g^{-1}
Zn$_x$Mo$_6$S$_8$ [145]	Mo$_6$S$_8$: Super-P: PVDF = 8:1:1	1 M ZnSO$_4$	0.50&0.35	134 mAh g^{-1} at 6.4 mA g^{-1}	/
Mo$_6$S$_8$ [146]	Mo$_6$S$_8$: Super-C: PVDF = 8:1:1	1 M ZnSO$_4$	0.50&0.34	63 mAh g^{-1} at 180 mA g^{-1}	95% retained after 150 cycles at 180 mA g^{-1}
Na$_3$V$_2$(PO$_4$)$_3$ [151]	Na$_3$V$_2$(PO$_4$)$_3$: acetylene black: PVDF = 8:2:1	0.5 M Zn(CH$_3$COO)$_2$	1.15	97 mAh g^{-1} at 0.5C	74% retained after 100 cycles at 0.5C
Na$_3$V$_2$(PO$_4$)$_2$F$_3$ [30]	Na$_3$V$_2$(PO$_4$)$_2$F$_3$: Super-P: PTFE = 7:2:1	2 M Zn(CH$_3$F$_3$SO$_3$)$_2$	1.62&1.35	60 mAh g^{-1} at 200 mA g^{-1}	95% retained after 4000 cycles at 1000 mA g^{-1}
Quinone (C4Q) [163]	C4Q: Super-P: PVDF = 6:3.5:0.5	3 M Zn(CH$_3$F$_3$SO$_3$)$_2$	1.00	335 mAh g^{-1} at 20 mA g^{-1}	87% retained after 1000 cycles at 500 mA g^{-1}
p-chloranil [165]	p-chloranil: Super-P: CMC/SBR(2:1) = 6:3.5:0.5	1 M Zn(OTf)$_2$-H$_2$O	1.10	200 mAh g^{-1} at 217 mA g^{-1}	53% retained after 100 cycles at 43.4 mA g^{-1}

performances of cathode materials. We have summarized the synthesis methods and synthesis conditions of various cathode materials with different structures for RZIBs (Table 4), including microemulsion method, hydrothermal method, microwave-assisted hydrothermal method, electrodeposition method, thermal decomposition method and co-precipitation method, etc. Each synthesis method has unique advantages and functional features as well as disadvantages. Among various synthetic methods, the hydrothermal method not only is an easy route for obtaining cathode materials with high particle purity, good dispersity, good and controllable crystal shape, but also has low synthesis cost and low synthesis temperature. However, this method needs high technology and high equipment requirements, and has poor safety performance and long preparation period. So it is difficult to achieve mass production of cathode materials for RZIBs. Microwave-assisted hydrothermal method can effectively shorten the reaction time within a few hours and accelerate the reaction process of synthesis. Most liquid methods, such as microemulsion method, electrodeposition method and co-precipitation method, etc. do not require high processing temperatures, expensive and complicated laboratory equipment, but have low particle purity, poor dispersity and crystal shape as well as sinterability. The results show that the type (e.g. nanorod or nanowire) of final cathode material for RZIBs determined the choice of synthesis methods. Although the synthesis technologies of cathode materials for RZIBs have been developed rapidly in recent years, there is a great need to develop new methods for synthesizing nanostructured electrodes with large inter-layer spacing. Table 5 is the electrochemical performances of RZIBs based on various cathodes and electrolytes.

According to this overview, further research directions and perspectives regarding the development of high performance RZIBs are proposed as follows: (1) The larger electrostatic interaction of the Zn cation with its surrounding electrolyte and electrode materials leads to extremely slow intercalation kinetics. A good method to solve this problem is synthesizing nano-sized materials. Nano-sized electrodes intrinsically benefit rapid ionic diffusion due to short transport distance and better accommodate the structural strain through slippage at domain boundaries. (2) Tailoring crystal orientation for electrode materials is also an attractive strategy because the exposure of specific planes of crystal structure promotes ionic transports on its exposure surface, further demonstrating high discharge capacity as well as high rate capability [168,169]. (3) It's worth noting that cation-defective materials by using cation nonstoichiometry can open up additional pathways for easier migration of multivalent metal-ions, which endue us another chance to acquire advanced electrode materials. (4) The emergence of flexible and wearable RZIBs provides a new opportunity for the application in wearable devices. Under this circumstance, RZIBs need to sustain harsher conditions such as folding, hitting puncture, tearing or immersion in water while exhibit a superior performance [170,171]. For example, Li et al. [172] fabricated an extremely safe, wearable and solid-state RZIB using novel gelatin and polyacrylamide (PAM) based hierarchical polymer electrolyte (HPE) and α-MnO₂ nanorod/carbon nanotube (CNT) cathode. This RZIB delivers superior specific capacity of 306 mAh g^{-1} and 97% capacity retention after 1000 cycles under various severe conditions, which is able to power a commercial smart watch and a wearable pulse sensor. Li et al. [173] prepared MoS₂ (E-MoS₂) cathode with the expanded inter-layer spacing by an electrodeposition approach and constructed a flexible solid-state RZIB based on this cathode, new Starch/PAM hydrogel electrolyte, and Zn anode. The Starch/PAM hydrogel electrolyte with a 3D porous architecture contributes to a high water-retention capability and fast ion diffusion. This battery shows a specific discharge capacity of 199.3 mAh g^{-1} at 100 mA g^{-1} and capacity retention is 97.7% over 500 cycles at 1000 mAg^{-1}. Furthermore, it also has high flexibility, mechanical robustness and electrochemical stability under various deformation conditions. Zhang et al. [174] designed a coaxial-fiber aqueous RZIB by adopting Zn nanosheet arrays on carbon nanotube fiber as the core electrode and spherical zinc hexacyanoferrate (ZnHCF) composite on

aligned carbon nanotube sheets as the outer electrode with ZnSO₄-carboxymethyl cellulose sodium gel electrolyte. This RZIB delivers excellent flexibility with the capacity retention of 93.2% after bending 3000 times. Wang et al. [175] fabricated a novel wire-shaped flexible RZIB based on Nitinol shape memory wire, stainless steel yarn and gelatin-borax complex electrolyte. Zinc anode and MnO₂ cathode are electrodeposited onto Nitinol wire and stainless steel yarn, respectively. Impressively, this flexible wire-shaped battery could recover both the shape and the electrochemical performances for multiple times once being heavily bended with permanent strain due to the shape memory effect provided by the Nitinol wire, showing excellent durability and stability. All in all, we hope this review offers motivation and inspiration for researchers to discover novel cathode materials and narrow the gap for commercialization of low cost, safe and high energy density RZIBs.

Declaration of competing interest

The authors declare that they have no known competing financial interests or personal relationships that could have appeared to influence the work reported in this paper.

Acknowledgements

References

[1] Y. Wang, B. Liu, Q. Li, S. Cartmell, S. Ferrara, J. Power Sources 286 (2015) 330–345.
[2] G. Zubi, R. Dufo-López, M. Carvalho, G. Pasaoglu, Renew. Sustain. Energy Rev. 89 (2018) 292–308.
[3] N. Nitta, F. Wu, J.T. Lee, G. Yushin, Mater. Today 18 (2015) 252–264.
[4] G. Liang, X. Qin, J. Zou, L. Luo, Y. Wang, M. Wu, H. Zhu, G. Chen, F. Kang, B. Li, Carbon 127 (2018) 424–431.
[5] B. Luo, Y. Hu, X. Zhu, T. Qiu, L. Zhi, M. Xiao, H. Zhang, M. Zou, A. Cao, L. Wang, J. Mater. Chem. 6 (2018) 1462–1472.
[6] Y.J. Nam, D.Y. Oh, S.H. Jung, Y.S. Jung, J. Power Sources 375 (2018) 93–101.
[7] X. Tao, Y. Liu, W. Liu, G. Zhou, J. Zhao, D. Lin, C. Zu, O. Sheng, W. Zhang, H. W. Lee, Y. Cui, Nano Lett. 17 (2017) 2967–2972.
[8] A. Eftekhari, D.W. Kim, J. Power Sources 395 (2018) 336–348.
[9] J.S. Park, J. Kim, J.H. Jo, S.T. Myung, J. Mater. Chem. 6 (2018) 16627–16637.
[10] T. Liu, Y. Zhang, Z. Jiang, X. Zeng, J. Ji, Z. Li, X. Gao, M. Sun, Z. Lin, M. Ling, J. Zheng, C. Liang, Energy Environ. Sci. 12 (2019) 1512–1533.
[11] X. Hu, X. Sun, S.J. Yoo, B. Evanko, F. Fan, S. Cai, C. Zheng, W. Hu, G.D. Stucky, Nano Energy 56 (2019) 828–839.
[12] Y. Lee, J.K. Yoo, Y. Oh, H. Park, W. Go, S.T. Myung, J. Kim, J. Mater. Chem. 6 (2018) 17571–17578.
[13] M. Song, H. Tan, D. Chao, H.J. Fan, Adv. Funct. Mater. 28 (2018) 1802564.
[14] D. Selvakumaran, A. Pan, S. Liang, J. Mater. Chem. 7 (2019) 18209–18236.
[15] J. Ming, J. Guo, C. Xia, W. Wang, H.N. Alshareef, Mater. Sci. Eng. R 135 (2019) 58–84.
[16] V. Verma, S. Kumar, W. Manalastas Jr., R. Satish, M. Srinivasan, Adv. Sustain. Syst. 3 (2019) 1800111.
[17] M.M. Huie, D.C. Bock, E.S. Takeuchi, A.C. Marschilok, K.J. Takeuchi, Coord. Chem. Rev. 287 (2015) 15–27.
[18] X. Deng, Y. Xu, Q. An, F. Xiong, S. Tan, L. Wu, L. Mai, J. Mater. Chem. 7 (2019) 10644–10650.
[19] R.J. Gummow, G. Vamvounis, M.B. Kannan, Y. He, Adv. Mater. 30 (2018) 1801702.
[20] P. Padigi, G. Goncher, D. Evans, R. Solanki, J. Power Sources 273 (2015) 460–464.
[21] Q. Li, N.J. Bjerrum, J. Power Sources 110 (2002) 1–10.
[22] T. Cai, L. Zhao, H. Hu, T. Li, X. Li, S. Guo, Y. Li, Q. Xue, W. Xing, Z. Yan, L. Wang, Energy Environ. Sci. 11 (2018) 2341–2347.
[23] W. Liu, J. Hao, C. Xu, J. Mou, L. Dong, F. Jiang, Z. Kang, J. Wu, B. Jiang, F. Kang, Chem. Commun. 53 (2017) 6872–6874.
[24] H.B. Zhao, C.J. Hu, H.W. Cheng, J.H. Fang, Y.P. Xie, W.Y. Fang, T.N.L. Doan, T.K. A. Hoang, J.Q. Xu, P. Chen, Sci. Rep. 6 (2016) 25809.
[25] L. Chen, Q. An, L. Mai, Adv. Mater. Interfaces 6 (2019) 1900387.
[26] D.R. Gabe, J. Appl. Electrochem. 27 (1997) 908–915.
[27] X. Wang, F. Wang, L. Wang, M. Li, Y. Wang, B. Chen, Y. Zhu, L. Fu, L. Zha, L. Zhang, Y. Wu, W. Huang, Adv. Mater. 28 (2016) 4904–4911.
[28] J.F. Parker, C.N. Chervin, I.R. Pala, M. Machler, M.F. Burz, J.W. Long, D. R. Rolison, Science 356 (2017) 415–418.
[29] H. Li, C. Xu, C. Han, Y. Chen, C. Wei, B. Li, F. Kang, J. Electrochem. Soc. 162 (2015) A1439–A1444.

[30] W. Li, K. Wang, S. Cheng, K. Jiang, Energy Storage Mater. 15 (2018) 14–21.
[31] G. Fang, J. Zhou, A. Pan, S. Liang, ACS Energy Lett. 3 (2018) 2480–2501.
[32] Z. Liu, P. Bertram, F. Endres, J. Solid State Electrochem. 21 (2017) 2021.
[33] M. Petkovic, K.R. Seddon, L.P.N. Rebelo, C.S. Pereira, Chem. Soc. Rev. 40 (2011) 1383–1403.
[34] R.K. Guduru, J.C. Icaza, Nanomaterials 6 (2016) 41.
[35] L. Zhang, L. Chen, X. Zhou, Z. Liu, Sci. Rep. 5 (2015) 18263.
[36] W. Liang, L. Wang, H. Zhu, Y. Pan, Z. Zhu, H. Sun, C. Ma, A. Li, Sol. Energy Mater. Sol. Cells 180 (2018) 158–167.
[37] M. Cakici, R.R. Kakarla, F. Alonso-Marroquin, Chem. Eng. J. 309 (2017) 151–158.
[38] C.J. Raj, K.B.R. Varma, Electrochim. Acta 56 (2010) 649–656.
[39] P.K. Gupta, A. Bhandari, J. Bhattacharya, R.G.S. Pala, J. Phys. Chem. C 12 (2018) 211689–211700.
[40] S. Zhu, Li, J. Liu, H. Wang, T. Wang, Y. Zhang, L. Zhang, R.S. Ruoff, F. Dong, ACS Nano 12 (2018) 1033–1042.
[41] S. Devaraj, N. Munichandraiah, J. Phys. Chem. C 112 (2008) 4406–4417.
[42] C. Xu, B. Li, H. Du, F. Kang, Angew. Chem., Int. Ed. Engl. 51 (2012) 933–935.
[43] F.Y. Cheng, J. Chen, L. Gou, P.W. Shen, Adv. Mater. 17 (2005) 2753.
[44] C. Xu, S.W. Chiang, J. Ma, F. Kang, J. Electrochem. Soc. 160 (2013) A93–A97.
[45] L. Athouel, F. Moser, R. Dugas, O. Crosnier, D. Belanger, T. Brousse, J. Phys. Chem. C 112 (2008) 7270–7277.
[46] A.S. Poyraz, J. Huang, S. Cheng, L. Wu, X. Tong, Y. Zhu, A.C. Marschilok, K. J. Takeuchi, E.S. Takeuchi, J. Electrochem. Soc. 164 (2017) A1983–A1990.
[47] C. Xu, C. Wei, B. Li, F. Kang, Z. Guan, J. Power Sources 196 (2011) 7854–7859.
[48] B. Lee, C.S. Yoon, H.R. Lee, K.Y. Chung, B.W. Cho, S.H. Oh, Sci. Rep. 4 (2014) 6066.
[49] A.D. Wadsley, Nature 172 (1953) 1103–1104.
[50] A.D. Wadsley, Acta Crystallogr. 8 (1955) 165–172.
[51] B. Lee, H.R. Lee, H. Kim, K.Y. Chung, B.W. Cho, S.H. Oh, Chem. Commun. 51 (2015) 9265–9268.
[52] J.E. Post, Proc. Natl. Acad. Sci. U.S.A. 96 (1999) 3447–3454.
[53] W. Wang, B. Jiang, W. Xiong, H. Sun, Z. Lin, L. Hu, J. Tu, H. Zhu, S. Jiao, Sci. Rep. 3 (2013) 3383.
[54] M. Villalobos, B. Lanson, A. Manceau, B. Toner, G. Sposito, Am. Mineral. 91 (2006) 489–502.
[55] K.D. Kwon, K. Refson, G. Sposito, Geochem. Cosmochim. Acta 73 (2009) 1273–1284.
[56] B. Lee, H.R. Seo, H.R. Lee, C.S. Yoon, J.H. Kim, K.Y. Chung, B.W. Cho, S.H. Oh, ChemSusChem 9 (2016) 1–10.
[57] T. Takashima, K. Hashimoto, R. Nakamura, J. Am. Chem. Soc. 134 (2012) 18153–18156.
[58] W.K. Pang, V.K. Peterson, N. Sharma, C.F. Zhang, Z.P. Guo, J. Phys. Chem. C 118 (2014) 3976–3983.
[59] J.E. Greedan, N.P. Raju, A.S. Wills, C. Morin, S.M. Shaw, J.N. Reimers, Chem. Mater. 10 (1998) 3058–3067.
[60] J.C. Hunter, J. Solid State Chem. 39 (1981) 142–147.
[61] A. Moezzi, M.B. Cortie, A.M. McDonagh, Dalton Trans. 42 (2013) 14432–14437.
[62] H. Pan, Y. Shao, P. Yan, Y. Cheng, K.S. Han, Z. Nie, C. Wang, J. Yang, X. Li, P. Bhattacharya1, K.T. Mueller, J. Liu, Nat. Energy 1 (2016) 16039.
[63] F. Jiao, P.G. Bruce, Adv. Mater. 19 (2007) 657–660.
[64] D. Su, H.-J. Ahn, G. Wang, J. Mater. Chem. 1 (2013) 4845–4850.
[65] S. Islam, M.H. Alfaruqi, V. Mathew, J. Song, S. Kim, S. Kim, J. Jo, J.P. Baboo, D. T. Pham, D.Y. Putro, Y.K. Sun, J. Kim, J. Mater. Chem. 5 (2017) 23299–23309.
[66] N. Zhang, F. Cheng, J. Liu, L. Wang, X. Long, X. Liu, F. Li, J. Chen, Nat. Commun. 8 (2017) 405.
[67] J.H. Zeng, Y.F. Wang, Y. Yang, J. Zhang, J. Mater. Chem. 20 (2010) 10915–10918.
[68] V. Mathew, J. Lim, J. Kang, J. Gim, A.K. Rai, J. Kim, Electrochem. Commun. 13 (2011) 730–733.
[69] E. Chae, J. Gim, J. Song, S. Kim, V. Mathew, J. Han, S. Boo, J. Kim, RSC Adv. 3 (2013) 26328–26333.
[70] M.H. Alfaruqi, V. Mathew, J. Gim, S. Kim, J. Song, J.P. Baboo, S.H. Choi, J. Kim, Chem. Mater. 27 (2015) 3609–3620.
[71] W.I.F. David, M.M. Thackeray, P.G. Bruce, J.B. Goodenough, Mater. Res. Bull. 19 (1984) 99–106.
[72] W. Sun, F. Wang, S. Hou, C. Yang, X. Fan, Z. Ma, T. Gao, F. Han, R. Hu, M. Zhu, C. Wang, J. Am. Chem. Soc. 139 (2017) 9775–9778.
[73] M.H. Alfaruqi, J. Gim, S. Kim, J. Song, D.T. Pham, J. Jo, Z. Xiu, V. Mathew, J. Kim, Electrochem. Commun. 60 (2015) 121–125.
[74] S.D. Han, S. Kim, D. Li, V. Petkov, H.D. Yoo, P.J. Phillips, H. Wang, J.J. Kim, K. L. More, B. Key, R.F. Klie, J. Cabana, V.R. Stamenkovic, T.T. Fister, N. M. Markovic, A.K. Burrell, S. Tepavcevic, J.T. Vaughey, Chem. Mater. 29 (2017) 4874–4884.
[75] J. Muldoon, C.B. Bucur, T. Gregory, Chem. Rev. 114 (2014) 11683–11720.
[76] H.D. Yoo, I. Shterenberg, Y. Gofer, G. Gershinsky, N. Poura, D. Aurbach, Energy Environ. Sci. 6 (2013) 2265–2279.
[77] S.-D. Han, N.N. Rajput, X. Qu, B. Pan, M. He, M.S. Ferrandon, C. Liao, K. A. Persson, ACS Appl. Mater. Interfaces 8 (2016) 3021–3031.
[78] C. Yuan, Y. Zhang, Y. Pan, X. Liu, G. Wang, D. Cao, Electrochim. Acta 116 (2014) 404–412.
[79] C. Wei, C. Xu, B. Li, H. Du, F. Kang, J. Phys. Chem. Solids 73 (2012) 1487–1491.
[80] J. Lee, J.B. Ju, W.I. Cho, B.W. Cho, S.H. Oh, Electrochim. Acta 112 (2013) 138–143.
[81] Q. Gao, Z. Yuan, L. Dong, G. Wang, X. Yu, Electrochim. Acta 270 (2018) 417–425.
[82] M. Zhong, D. Yang, C. Xie, Z. Zhang, Z. Zhou, X.H. Bu, Small 12 (2016) 5564–5571.

[83] J.C. Knight, S. Therese, A. Manthiram, J. Mater. Chem. 3 (2015) 21077–21082.
[84] T. Koketsu, J. Ma, B.J. Morgan, M. Body, C. Legein, W. Dachraoui, M. Giannini, A. Demortière, M. Salanne, F. Dardoize, H. Groult, O.J. Borkiewicz, K. W. Chapman, P. Strasser, D. Dambournet, Nat. Mater. 16 (2017) 1142–1148.
[85] L. Sánchez, J.P. Pereira-Ramos, J. Mater. Chem. 7 (1997) 471–473.
[86] N. Zhang, F. Cheng, Y. Liu, Q. Zhao, K. Lei, C. Chen, X. Liu, J. Chen, J. Am. Chem. Soc. 138 (2016) 12894–12901.
[87] C. Li, X. Han, F. Cheng, Y. Hu, C. Chen, J. Chen, Nat. Commun. 6 (2015) 7345.
[88] L. Suo, O. Borodin, T. Gao, M. Olguin, J. Ho, X. Fan, C. Luo, C. Wang, K. Xu, Science 350 (2015) 938–943.
[89] Y. Yamada, K. Furukawa, K. Sodeyama, K. Kikuchi, M. Yaegashi, Y. Tateyama, A. Yamada, J. Am. Chem. Soc. 136 (2014) 5039–5046.
[90] X. Wu, Y. Xiang, Q. Peng, X. Wu, Y. Li, F. Tang, R. Song, Z. Liu, Z. He, X. Wu, J. Mater. Chem. 5 (2017) 17990–17997.
[91] S. Islam, M.H. Alfaruqi, J. Song, S. Kim, D.T. Pham, J. Jo, S. Kim, V. Mathew, J. P. Baboo, Z. Xiu, J. Kim, J. Energy Chem. 26 (2017) 815–819.
[92] B. Wu, G. Zhang, M. Yan, T. Xiong, P. He, L. He, X. Xu, L. Mai, Small 14 (2018) 1703850.
[93] G.G. Yadav, J.W. Gallaway, D.E. Turney, M. Nyce, J. Huang, X. Wei, S. Banerjee, Nat. Commun. 8 (2017) 14424.
[94] D. Xu, B. Li, C. Wei, Y.B. He, H. Du, X. Chu, X. Qin, Q.H. Yang, F. Kang, Electrochim. Acta 133 (2014) 254–261.
[95] D. Imamura, Solid State Ion. 161 (2003) 173–180.
[96] S. Gu, H. Wang, C. Wu, Y. Bai, H. Li, F. Wu, Energy Storage Mater. 6 (2017) 9–17.
[97] J. Zhou, L. Shan, Z. Wu, X. Guo, G. Fang, S. Liang, Chem. Commun. 54 (2018) 4457–4460.
[98] P. Hu, M. Yan, T. Zhu, X. Wang, X. Wei, J. Li, L. Zhou, Z. Li, L. Chen, L. Mai, ACS Appl. Mater. Interfaces 9 (2017) 42717–42722.
[99] L. Suo, O. Borodin, W. Sun, X. Fan, C. Yang, F. Wang, T. Gao, Z. Ma, M. Schroeder, A. Gresce, S. Russell, M. Armand, A. Angell, K. Xu, C. Wang, Angew. Chem. Int. Ed. 55 (2016) 7136–7141.
[100] A. Gambou-Bosca, D. Bélanger, J. Power Sources 326 (2016) 595–603.
[101] Y. Zhao, C. Han, J. Yang, J. Su, X. Xu, S. Li, L. Xu, R. Fang, H. Jiang, X. Zou, B. Song, L. Mai, Q. Zhang, Nano Lett. 15 (2015) 2180–2185.
[102] P. Senguttuvan, S.D. Han, S. Kim, A.L. Lipson, S. Tepavcevic, T.T. Fister, I. D. Bloom, A.K. Burrell, C.S. Johnson, Adv. Energy Mater. 6 (2016) 1600826.
[103] S. Tepavcevic, Y. Liu, D. Zhou, B. Lai, J. Maser, X. Zuo, H. Chan, P. Král, C. S. Johnson, V. Stamenkovic, N.M. Markovic, T. Rajh, ACS Nano 9 (2015) 8194–8205.
[104] H.Y. Li, C.H. Yang, C.M. Tseng, S.W. Lee, C.C. Yang, T.Y. Wu, J.K. Chang, J. Power Sources 285 (2015) 418–424.
[105] M. Yan, P. He, Y. Chen, S. Wang, Q. Wei, K. Zhao, X. Xu, Q. An, Y. Shuang, Y. Shao, K.T. Mueller, L. Mai, J. Liu, J. Yang, Adv. Mater. 30 (2017) 1703725.
[106] K.W. Nam, H. Kim, J.H. Choi, J.W. Choi, Energy Environ. Sci. 12 (2019) 1999–2009.
[107] D. Kundu, B.D. Adams, V. Duffort, S.H. Vajargah, L.F. Nazar, Nat. Energy 1 (2016) 16119.
[108] C. Xia, J. Guo, P. Li, X. Zhang, H.N. Alshareef, Angew. Chem. Int. Ed. 57 (2018) 3943–3948.
[109] P. He, G. Zhang, X. Liao, M. Yan, X. Xu, Q. An, J. Liu, L. Mai, Adv. Energy Mater. 8 (2018) 1702463.
[110] L. Shan, Y. Yang, W. Zhang, H. Chen, G. Fang, J. Zhou, S. Liang, Energy Storage Mater. 18 (2019) 10–14.
[111] V. Bodenez, L. Dupont, M. Morcrette, C. Surcin, D.W. Murphy, J.M. Tarascon, Chem. Mater. 18 (2006) 4278–4287.
[112] K. Kirshenbaum, D.C. Bock, C.Y. Lee, Z. Zhong, K.J. Takeuchi, A.C. Marschilok, E. S. Takeuchi, Science 347 (2015) 149–154.
[113] E.S. Takeuchi, A.C. Marschilok, K.J. Takeuchi, A. Ignatov, Z. Zhong, M. Croft, Energy Environ. Sci. 6 (2013) 1465–1470.
[114] L. Shan, J. Zhou, M. Han, G. Fang, X. Cao, X. Wu, S. Liang, J. Mater. Chem. 7 (2019) 7355–7359.
[115] F. Ming, H. Liang, Y. Lei, S. Kandambeth, M. Eddaoudi, H.N. Alshareef, ACS Energy Lett. 3 (2018) 2602–2609.
[116] Y. Fang, Y. Tang, G. Fang, L. Shan, J. Guo, W. Zhang, J. Zhou, C. Wang, L. Wang, S. Liang, Energy Environ. Sci. 11 (2018) 3157–3162.
[117] C. Xia, J. Guo, Y. Lei, H. Liang, C. Zhao, H.N. Alshareef, Adv. Mater. 30 (2018) 1705580.
[118] W. Kaveevivitchai, A. Manthiram, J. Mater. Chem. 4 (2016) 18737–18741.
[119] J.H. Jo, Y.K. Sun, S.T. Myung, J. Mater. Chem. 5 (2017) 8367–8375.
[120] M.H. Alfaruqi, V. Mathew, J. Song, S. Kim, J.P. Baboo, Z. Xiu, K.S. Lee, Y.K. Sun, J. Kim, Chem. Mater. 29 (2017) 1684–1694.
[121] P. He, Y. Quan, X. Xu, M. Yan, W. Yang, Q. An, L. He, L. Mai, Small 13 (2017) 1702551.
[122] P. Hu, T. Zhu, X. Wang, X. Wei, M. Yan, J. Li, W. Luo, W. Yang, W. Zhang, L. Zhou, Z. Zhou, L. Mai, Nano Lett. 18 (2018) 1758–1763.
[123] F. Wan, L. Zhang, X. Dai, X. Wang, Z. Niu, J. Chen, Nat. Commun. 9 (2018) 1656.
[124] B. Tang, G. Fang, J. Zhou, L. Wang, Y. Lei, C. Wang, T. Lin, Y. Tang, S. Liang, Nano Energy 51 (2018) 579–587.
[125] X. Guo, G. Fang, W. Zhang, J. Zhou, L. Shan, L. Wang, C. Wang, T. Lin, Y. Tang, S. Liang, Adv. Energy Mater. 8 (2018) 1801819.
[126] H. Li, T. Zhai, P. He, Y. Wang, E. Hosono, H. Zhou, J. Mater. Chem. 21 (2011) 1780–1787.
[127] G. Fang, S. Liang, Z. Chen, P. Cui, X. Zheng, A. Pan, B. Lu, X. Lu, J. Zhou, Adv. Funct. Mater. 29 (2019) 1905267.
[128] A. Kumar, S.M. Yusuf, L. Keller, Phys. Rev. B 71 (2005), 054414.

[129] P. Padigi, J. Thiebes, M. Swan, G. Goncher, D. Evans, Electrochim. Acta 166 (2015) 32–39.
[130] H. Lee, Y.I. Kim, J.K. Park, J.W. Choi, Chem. Commun. 48 (2012) 8416–8418.
[131] P. Nie, L. Shen, H. Luo, B. Ding, G. Xu, J. Wang, X. Zhang, J. Mater. Chem. 2 (2014) 5852–5857.
[132] S. Liu, G.L. Pan, G.R. Li, X.P. Gao, J. Mater. Chem. 3 (2015) 959–962.
[133] R.Y. Wang, C.D. Wessells, R.A. Huggins, Y. Cui, Nano Lett. 13 (2013) 5748–5752.
[134] L. Zhang, L. Chen, X. Zhou, Z. Liu, Adv. Energy Mater. 5 (2014) 1400930.
[135] J.J. Alexander, H.B. Gray, J. Am. Chem. Soc. 90 (1968) 4260–4271.
[136] R. Trócoli, F.L. Mantia, ChemSusChem 8 (2015) 481–485.
[137] M.S. Chae, J.W. Heo, H.H. Kwak, H. Lee, S.T. Hong, J. Power Sources 337 (2017) 204–211.
[138] Z. Liu, G. Pulletikurthi, F. Endres, ACS Appl. Mater. Interfaces 8 (2016) 12158–12164.
[139] M. Pasta, C.D. Wessells, N. Liu, J. Nelson, M.T. McDowell, R.A. Huggins, M. F. Toney, Y. Cui, Nat. Commun. 5 (2014) 3007.
[140] E. Levi, G. Gershinsky, D. Aurbach, O. Isnard, G. Ceder, Chem. Mater. 21 (2009) 1390–1399.
[141] S. Belin, R. Chevrel, M. Sergent, J. Solid State Chem. 155 (2000) 250–258.
[142] J.H. Cho, J.H. Ha, J.G. Lee, C.S. Kim, B.W. Cho, K.B. Kim, K.Y. Chung, J. Phys. Chem. C 121 (2017) 12617–12623.
[143] J. Barbosa, C. Prestipino, O.J. Hernandez, S. Paofai, C. Dejoie, M.G. Viry, C. Boulanger, Inorg. Chem. 58 (2019) 2158–2168.
[144] S. Seghir, C. Boulanger, S. Diliberto, J.M. Lecuire, M. Potel, O.M. Conanec, Electrochem. Commun. 10 (2008) 1505–1508.
[145] M.S. Chae, J.W. Heo, S.C. Lim, S.T. Hong, Inorg. Chem. 55 (2016) 3294–3301.
[146] Y. Cheng, L. Luo, L. Zhong, J. Chen, B. Li, W. Wang, S.X. Mao, C. Wang, V. L. Sprenkle, G. Li, J. Liu, ACS Appl. Mater. Interfaces 8 (2016) 13673–13677.
[147] Z. Jian, Y.S. Hu, X. Ji, W. Chen, Adv. Mater. 29 (2017) 1601925.
[148] C. Masquelier, L. Croguennec, Chem. Rev. 113 (2013) 6552–6591.
[149] P.N. Didwal, R. Verma, C.W. Min, C.J. Park, J. Power Sources 413 (2019) 1–10.
[150] X. Liu, E. Wang, G. Feng, Z. Wu, W. Xiang, X. Guo, J. Li, B. Zhong, Z. Zheng, Electrochim. Acta 286 (2018) 231–241.
[151] G. Li, Z. Yang, Y. Jiang, C. Jin, W. Huang, X. Ding, Y. Huang, Nano Energy 25 (2016) 211–217.
[152] W. Song, X. Ji, Z. Wu, Y. Yang, Z. Zhou, F. Li, Q. Chen, C.E. Banks, J. Power Sources 256 (2014) 258–263.
[153] W. Song, Z. Wu, J. Chen, Q. Lan, Y. Zhu, Y. Yang, C. Pan, H. Hou, M. Jing, X. Ji, Electrochim. Acta 146 (2014) 142–150.
[154] J. Feng, X. Sun, C. Wu, L. Peng, C. Lin, S. Hu, J. Yang, Y. Xie, J. Am. Chem. Soc. 133 (2011) 17832–17838.
[155] C. Zhao, C. Yu, M. Zhang, Q. Sun, S. Li, M.N. Banis, X. Han, Q. Dong, J. Yang, G. Wang, X. Sun, J. Qiu, Nano Energy 41 (2017) 66–74.
[156] P. He, M. Yan, G. Zhang, R. Sun, L. Chen, Q. An, L. Mai, Adv. Energy Mater. 7 (2017) 1601920.
[157] H. Liang, Z. Cao, F. Ming, W. Zhang, D.H. Anjum, Y. Cui, L. Cavallo, H. N. Alshareef, Nano Lett. 19 (2019) 3199–3206.
[158] W. Xu, C. Sun, K. Zhao, X. Cheng, S. Rawal, Y. Xu, Y. Wang, Energy Storage Mater. 16 (2019) 527–534.
[159] K. Lin, Q. Chen, M.R. Gerhardt, L. Tong, S.B. Kim, L. Eisenach, A.W. Valle, D. Hardee, R.G. Gordon, M.J. Aziz, M.P. Marshak, Science 349 (2015) 1529–1532.
[160] T.B. Schon, B.T. McAllister, P.-F. Li, D.S. Seferos, Chem. Soc. Rev. 45 (2016) 6345–6404.
[161] Y. Liang, Y. Jing, S. Gheytani, K.-Y. Lee, P. Liu, A. Facchetti, Y. Yao, Nat. Mater. 16 (2017) 841–848.
[162] X. Dong, L. Chen, J. Liu, S. Haller, Y. Wang, Y. Xia, Sci. Adv. 2 (2016), e1501038.
[163] Q. Zhao, W. Huang, Z. Luo, L. Liu, Y. Lu, Y. Li, L. Li, J. Hu, H. Ma, J. Chen, Sci. Adv. 4 (2018) 2375–2548.
[164] B.S. Creaven, D.F. Donlon, J. McGinley, Coord. Chem. Rev. 253 (2009) 893–962.
[165] D. Kundu, P. Oberholzer, C. Glaros, A. Bouzid, E. Tervoort, A. Pasquarello, M. Niederberger, Chem. Mater. 30 (2018) 3874–3881.
[166] A. Khayum, M. Ghosh, V. Vijayakumar, A. Halder, M. Nurhuda, S. Kumar, M. Addicoat, S. Kurungot, R. Banerjee, Chem. Sci. 10 (2019) 8889–8894.
[167] X. Wang, L. Chen, F. Lu, J. Liu, X. Chen, G. Shao, ChemElectroChem 6 (2019) 3644–3647.
[168] F. Wang, X. Wang, Z. Chang, Y. Zhu, L. Fu, X. Liu, Y. Wu, Y. Wu, W. Huang, A. Subramanian, H. Fan, L. Qi, A. Kushima, J. Li, Y. Lin, K. Xu, L.W. Wang, Y. P. Wu, F. Pan, Nanoscale Horiz. 1 (2016) 272–289.
[169] L. Wang, X. He, W. Sun, J. Wang, Y. Li, S. Fan, Nano Lett. 12 (2012) 5632–5636.
[170] A. Konarov, N. Voronina, J.H. Jo, Z. Bakenov, Y.K. Sun, S.T. Myung, ACS Energy Lett. 3 (2018) 2620–2640.
[171] P.H. Yang, K. Liu, Q. Chen, X.B. Mo, Y.S. Zhou, S. Li, G. Feng, J. Zhou, Angew. Chem. Int. Ed. 55 (2016) 12050–12053.
[172] H. Li, C. Han, Y. Huang, Y. Huang, M. Zhu, Z. Pei, Q. Xue, Z. Wang, Z. Liu, Z. Tang, Y. Wang, F. Kang, B. Li, C. Zhi, Energy Environ. Sci. 11 (2018) 941–951.
[173] H. Li, Q. Yang, F. Mo, G. Liang, Z. Liu, Z. Tang, L. Ma, J. Liu, Z. Shi, C. Zhi, Energy Storage Mater. 19 (2019) 94–101.
[174] Q. Zhang, C. Li, Q. Li, Z. Pan, J. Sun, Z. Zhou, B. He, P. Man, L. Xie, L. Kang, X. Wang, J. Yang, T. Zhang, P.P. Shum, Q. Li, Y. Yao, L. Wei, Nano Lett. 19 (2019) 4035–4042.
[175] Z. Wang, Z. Ruan, Z. Liu, Y. Wang, Z. Tang, H. Li, M. Zhu, T.F. Hung, J. Liu, Z. Shi, C. Zhi, J. Mater. Chem. 6 (2018) 8549–8557.